

## REPORT DOCUMENTATION PAGE

The public reporting burden for this collection of information is estimated to average 1 hour per response, including the time for reviewing instructions, searching existing data sources, gathering and maintaining the data needed, and completing and reviewing the collection of information. Send comments regarding this burden estimate or any other aspect of this collection of information, including suggestions for reducing the burden, to Department of Defense, Washington Headquarters Services, Directorate for Information Operations and Reports (0704-0188), 1215 Jefferson Davis Highway, Suite 1204, Arlington, VA 22202-4302. Respondents should be aware that notwithstanding any other provision of law, no person shall be subject to any penalty for failing to comply with a collection of information if it does not display a currently valid OMB control number.

PLEASE DO NOT RETURN YOUR FORM TO THE ABOVE ADDRESS.

|  |             |                                     |                               |  |   |
|--|-------------|-------------------------------------|-------------------------------|--|---|
| 1. REPORT DATE (DD-MM-YYYY)<br>27/01/2009  |             | 2. REPORT TYPE<br>Final Performance |                               | 3. DATES COVERED (From - To)<br>15-03-06 to 30-11-08 |   |
| 4. TITLE AND SUBTITLE<br>The Analysis and Modeling of Phase Stability and Multiphase Designs in High Temperature Refractory Metal-Silicon-Boron Alloys   |             |                                     |                               | 5a. CONTRACT NUMBER                                  |   |
|  |             |                                     |                               | 5b. GRANT NUMBER<br>FA9550-06-1-0233                 |   |
|  |             |                                     |                               | 5c. PROGRAM ELEMENT NUMBER                           |   |
|  |             |                                     |                               | 5d. PROJECT NUMBER                                   |   |
| 6. AUTHOR(S)<br>Professor John H. Perepezko  |             |                                     |                               | 5e. TASK NUMBER                                      |   |
|  |             |                                     |                               | 5f. WORK UNIT NUMBER                                 |   |
|  |             |                                     |                               |  |   |
| 7. PERFORMING ORGANIZATION NAME(S) AND ADDRESS(ES)<br>University of Wisconsin-Madison<br>Research and Sponsored Programs<br>750 University Ave.<br>Madison, WI 53706-1141  |             |                                     |                               | 8. PERFORMING ORGANIZATION<br>REPORT NUMBER          |   |
| 9. SPONSORING/MONITORING AGENCY NAME(S) AND ADDRESS(ES)<br>Air Force Office of Scientific Research<br>Research/NA (Dr. J. Fuller)<br>High Temperature Aerospace Materials<br>875 North Randolph Street<br>Arlington, Virginia 22203  |             |                                     |                               | 10. SPONSOR/MONITOR'S ACRONYM(S)                     |   |
|  |             |                                     |                               | 11. SPONSOR/MONITOR'S REPORT<br>NUMBER(S)            |   |
| 12. DISTRIBUTION/AVAILABILITY STATEMENT<br><br>Distribution A: Approved for Public Release   |             |                                     |                               |  |   |
| 13. SUPPLEMENTARY NOTES  |             |                                     |                               |  |   |
| 14. ABSTRACT<br>For high temperature application beyond the range of Ni-base superalloys, Mo-Si-B alloys with the ternary intermetallic, Mo <sub>5</sub> SiB <sub>2</sub> , T <sub>2</sub> phase as a key microstructure constituent, offer an attractive property balance of high melting temperature, oxidation resistance and useful high temperature mechanical properties. The fundamental basis of the alloying behavior in T <sub>2</sub> including the mutual solid solution with transition metals has been established in terms of the governing geometric and electronic factors. For non-stoichiometric compositions, constitutional defects such as vacancies for Mo-rich compositions control the homogeneity range and play a key role in the development of dislocation and precipitation reactions that directly impact high temperature structural performance. The sluggish diffusion rates within the T <sub>2</sub> phase have also been quantified and applied to materials processing strategies. The materials design based on the phase stability, diffusion and defect structure analysis in the Mo-Si-B system can also be applied to the design of new multiphase high-temperature alloys with balanced environmental and mechanical properties. |             |                                     |                               |  |   |
| 15. SUBJECT TERMS<br>Phase Stability, Alloying, High Temperature, Defect Structure, Mo Alloys, Microstructure, Diffusion   |             |                                     |                               |  |   |
| 16. SECURITY CLASSIFICATION OF:  |             |                                     | 17. LIMITATION OF<br>ABSTRACT | 18. NUMBER<br>OF<br>PAGES                            | 19a. NAME OF RESPONSIBLE PERSON           |
| a. REPORT  | b. ABSTRACT | c. THIS PAGE                        |                               |  | 19b. TELEPHONE NUMBER (Include area code) |
| U  | U           | U                                   | UU                            | 41   |   |

20090324167

## TABLE OF CONTENTS

|   |    |
|---|----|
| <b>1. <u>Introduction</u></b>   | 2  |
| <b>2. <u>Research Highlights</u></b>  |    |
| 2.1. Phase Stability and Structural Defects in Refractory Metal Silicides               | 2  |
| 2.2. Structures of Metal-Rich Silicide and Borosilicide Phases                          | 3  |
| 2.3. High Temperature Phase Equilibria in the Mo-Si-B System                            | 4  |
| 2.4. Phase Stability Relation to Processing   | 5  |
| 2.5. Thermodynamic Modeling in Mo-Si-B and Mo-TM-Si-B Systems                           | 6  |
| 2.6. Kinetic Behavior in the $T_2$ Phase  | 7  |
| 2.7. Annealing Response of Constitutional Vacancies and Dislocations in the $T_2$ phase | 8  |
| 2.8. Alloying behavior in $T_2$ Phase   | 11 |
| 2.9. Evaluation of Phase Stability  | 11 |
| 2.10. Structural Stability of the $T_2$ Phase   | 13 |
| 2.10.1 Geometric Factors  | 13 |
| 2.10.2. Electronic Factors in Phase Stability   | 14 |
| 2.11 Multiphase Microstructure Design   | 16 |
| 2.12. BCC + $T_2$ + $T_1$ Ultra-high Temperature Three-Phase Alloys                     | 17 |
| <b>3. <u>Summary of Research Highlights</u></b>   | 19 |
| <b>4. <u>Personnel Supported</u></b>  | 20 |
| <b>5. <u>Publication List</u></b>   | 21 |
| <b>6. <u>Transitions</u></b>  | 21 |
| <b>7. <u>Patents</u></b>  | 21 |
| <b>8. <u>Honors/Awards</u></b>  | 21 |
| <b>9. <u>References</u></b>   | 21 |
| <b>10. <u>Figures</u></b>   | 25 |

## **1. Introduction**

In many respects high temperature materials play a pivotal role as enabling materials for a number of key technologies such as transportation and energy. Without Ni base superalloys the current generation of gas turbine engines would not be possible. Similarly, without creep and oxidation resistant ferritic steels, energy generation would not be cost effective. At the same time, the performance requirements in terms of operating temperature and lifetime are increasing and the near term projections clearly exceed the capabilities of the current materials. While the trend of increasing performance demands is not new, high temperature materials such as Ni base superalloys have been able to meet the need for increasing performance by incremental improvement in capability based upon innovative microstructure control, multicomponent alloying and by the introduction of sophisticated thermal management by thermal barriers and internal cooling. In spite of the remarkable and impressive nature of the advances, the enhancements highlight a clear trend of a trade off between higher operating temperature and a steadily falling increase in efficiency [03DIM]. Moreover, Ni base alloys are already operating at 0.85 of the melting temperature so that any further improvement in operating temperature is limited. With such a trend it is also clear that new materials with much higher melting temperature than Ni base systems are needed for any significant improvement in operating temperature and efficiency.

For metallic systems, the refractory metals such as Mo and Nb meet the requirement of high melting temperature. However, both Mo and Nb develop non-protective oxides and Nb has a high solubility for oxygen and nitrogen [97PER]. Fortunately, for Mo-base systems silicide intermetallic phases that develop protective  $\text{SiO}_2$  coatings upon oxidation have been identified [03DIM, 07PER, 97PET] and can be treated further to provide a robust environmental protection over a wide temperature range. The Mo-Si-B system has attracted the most attention and is the focus of the present prospective on the phase stability [03DIM, 97PER, 07PER].

## **2. Research Highlights**

### **2.1. Phase Stability and Structural Defects in Refractory Metal Silicides**

Refractory metals (RM) are represented by the high melting point transition metal (TM) elements from group VB- VIIB and some of the late group VIII members from the periodic table. The BCC refractory metals from the VB and VIB elements form a number of intermediate phases of interest including several types of refractory-metal rich silicides and borosilicides (i.e.  $[\text{RM}] > 60 \text{ at. \%}$ ) that have attracted attention for high temperature structural applications. Even though the refractory metals often form similar silicide phases in terms of stoichiometry and related crystal structures, the elevated temperature performance and oxidation resistance vary widely. The 5-3 metal-rich silicides  $\text{RM}_5\text{Si}_3$  or the borosilicide variant of  $\text{RM}_5\text{Si}_{(1+x)}\text{B}_{(2-x)}$  ( $x = 0-1$ ) have been included in microstructural designs that yield useful structural performance, since they have a high thermal stability due to the mixed metallic and covalent bonding within their complex crystal structures [94MCM] and they can be in equilibrium with their respective refractory metals to form a stable a two-phase field of  $\text{RM} + \text{RM}_5(\text{Si},\text{B})_3$ . Within this group there are structural types with a stoichiometry of  $\text{RM}_5\text{Si}_3$  in binary systems, but comparable structures are found in ternary alloys where there is a partial or complete substitution of Si by B as represented by  $\text{RM}_5(\text{Si},\text{B})_3$ ,  $\text{RM}_5\text{SiB}_2$  or  $\text{RM}_5\text{B}_3$ . The representative structures include the  $T_1$ ,  $T_2$  and  $D8_8$  phases.



## 2.2. Structures of Metal-Rich Silicide and Borosilicide Phases

For the examination on the stability of the silicide and borosilicide phases, it is useful to examine the relevant crystal structures at the stoichiometric composition. The approach to phase stability analysis in metal-metalloid intermetallics in general has been based on the stacking of atomic layers within the crystal structure [60PAU, 31HAG]. The  $\text{Mo}_5\text{SiB}_2$  ( $T_2$ ) crystal has a  $D8_1$  structure that forms a body-centered tetragonal unit cell (space group 14/mcm). A 3-dimensional drawing of the  $T_2$  ( $\text{Mo}_5\text{SiB}_2$ ) structure is shown in Figure 1. The unit cell contains 32 atoms (20 Mo, 4 Si and 8 B atoms) that are situated in layered arrangements along the  $c$  axis. From the previous work [57NOW, 58ARO, 59ARO, 57NOW, 60NOW, 84FRA], three types of layers have been identified: layer A with only Mo atoms, layer B with only Si atoms and layer C with a mixture of Mo and B atoms. The structural arrangement of these layers in  $T_2$  has been viewed as the means to achieve an efficient atomic packing between metal atoms such as Mo and metalloid constituents (Si and B in this case) [57NOW, 58ARO, 59ARO, 57NOW, 60NOW]. Based on the radius ratio of the metal atom and the metalloid atoms, variations in the successive stacking based on the A layered arrangement can be constructed [31HAG]. The relatively large difference in atomic radius of the two types of metalloids necessitates stacking arrangements of the A layers that would facilitate two distinct sites. Layer arrangements of  $A - A_{1/2/1/2} - A_{1/2/1/2} - A - A_{1/2/1/2}$  in the  $[001]$  direction are therefore developed in the  $T_2$  structure. The  $A_{1/2/1/2}$  layer refers to the A layer that has been translated by half the base diagonal relative to neighboring layers. With the  $A - A_{1/2/1/2}$  or vice versa, a cubic anti-prismatic site is created and filled by Si atoms forming the layer C (see Figure 1). The B atoms on the other hand are situated in the trigonal prismatic hole generated by sandwiching two symmetrically oriented A layers (the  $A - A$  or  $A_{1/2/1/2} - A_{1/2/1/2}$  layer arrangements). In this arrangement, the B atoms are capped by two triangular arrangements of Mo atoms along the  $c$  axis and one B and two more Mo atoms forming an intermediate layer (layer C). The two Mo atoms fill the remaining available hole created by the  $A - A$  layer arrangements that accordingly constitutes the largest hole available (the cubic prismatic hole). Thus, the limited ability to stabilize the  $T_2$  phase in the Si-rich region for the Mo-Si-B system may be interpreted as the difficulty in situating Si atoms in the B sub-lattice in the trigonal prismatic hole site. On the other hand, there is a ready accommodation of B atoms in the Si lattice position which is also indicated by the reduction of the cell volume. Moreover, this behavior is directly correlated with the available cell volume within the  $T_2$  phase homogeneity range and is consistent with the observed asymmetric homogeneity range.

The A layer arrangement in the  $T_2$  phase is not necessarily unique since it is also observed in both borides ( $\text{Mo}_2\text{B}$ ) and silicides ( $T_1$ ). In fact, the stacking arrangements of the different layer types are part of the larger crystal family of  $\text{CuAl}_2$ -type phases where the radius ratio of the metal to metalloids determine (from the geometric point of view) the types of stacking within the crystal structure. The  $T_2$  phase has the atomic radius ratio 'in-between' the known silicides and borides with comparable amount of metal content (i.e.  $\text{Mo}_2\text{B}$  and  $\text{Mo}_5\text{Si}_3$ ). The  $\text{Mo}_2\text{B}$  has a higher radius ratio of metal to metalloid than the  $\text{Mo}_5\text{SiB}_2$  and it has only one type of metalloid site. Previous studies suggested that due to this relatively high radius ratio, the boride phase forms a repeated  $A - A_{1/2/1/2}$  atomic stacking (instead of  $A - A_{1/2/1/2} - A_{1/2/1/2} - A$  stacking sequence in  $T_2$  phase)[60PAU, 59ARO, 84FRA]. With the repeated  $A - A_{1/2/1/2}$  layer stacking, only one type of interstitial site (anti-prismatic hole) can be created (i.e. the "Si site" in

Mo<sub>5</sub>SiB<sub>2</sub>). The Mo<sub>5</sub>Si<sub>3</sub> (T<sub>1</sub> phase) on the other hand has a radius ratio of metal to metalloid below that of T<sub>2</sub> phase. The normal A – A<sub>1/2</sub> atomic stacking to fill in Si atoms is accommodated by replacing part of the Mo “A” layers by vacancies and Si atoms to form a modified A layer. Hence, in the T<sub>1</sub> phase, there are two types of the Si atoms, one that is sandwiched between the modified A and A<sub>1/2</sub> layers and the one that is within the modified A layers (see Figure 2 and 3). In both Mo<sub>2</sub>B and T<sub>1</sub>, the crystal structures do not stabilize the A-A layered arrangement.

In this context, it is worthwhile to note another crystal variant of the T<sub>2</sub> crystal structure, namely the D8<sub>8</sub> phase (Figure 4). Similar to the Mo<sub>2</sub>B and T<sub>1</sub> phases, the D8<sub>8</sub> phase also has alternating atomic layer stacking of ‘modified’ A layer and A<sub>1/2</sub> layer. The difference is that the modified A layer forms a hexagonal base symmetry instead of a tetragonal one (like in Mo<sub>2</sub>B, T<sub>1</sub> and T<sub>2</sub> phases). In addition, only half of the interstitial sites available from this type of configuration are filled by the metal constituent i.e. Ti in Ti<sub>5</sub>Si<sub>3</sub>. Unlike the T<sub>2</sub> phase, the D8<sub>8</sub> phase is most stable when the base metal is the Group IVB such as Ti or Hf. In the case of the Ti-Si-B system, there is a competing Ti-rich silicide phase termed the 6-2-1 phase (i.e. Ti<sub>6</sub>Si<sub>2</sub>B) [04RAM]. Among the 5-3 phases, the D8<sub>8</sub> structure has the highest solubility for interstitials such as C, N and O due to its relatively open crystal structure.

### 2.3. High Temperature Phase Equilibria in the Mo-Si-B System

The characteristics of the key phase structures provide a useful perspective to consider the phase equilibria in the Mo-Si-B system. The phase diagram isotherms for the Mo-rich portion of the Mo-Si-B system have been determined at various high temperatures (>1600°C). The isotherm at 1600°C is shown in Figure 5 along with the 1600°C isotherm for the Nb-Si-B system. Three-phase samples such as: [Mo(ss)-T<sub>2</sub>-Mo<sub>2</sub>B], [Mo<sub>2</sub>B-T<sub>2</sub>-MoB], [MoB-T<sub>2</sub>-Mo<sub>5</sub>Si<sub>3</sub>], [Mo<sub>5</sub>Si<sub>3</sub>-T<sub>2</sub>-Mo<sub>3</sub>Si] and [Mo<sub>3</sub>Si-T<sub>2</sub>-Mo(ss)] were equilibrated in the range of 1600 – 1950 °C. The EPMA examination on three-phase equilibrium samples allowed the determination of phase identities and the phase boundary compositions. For the compositions of interest in applications in the Mo(ss)+T<sub>2</sub>+Mo<sub>3</sub>Si three phase field the reported liquidus projection indicates that the primary phase is the Mo(ss) that then reacts on cooling to yield the T<sub>2</sub> phase and final solidification through a eutectic reaction to Mo(ss)+Mo<sub>3</sub>Si + T<sub>2</sub>. Due to the limited solubilities in the system, segregation is expressed as non-equilibrium phases and relative amounts [01PER]. The sluggish diffusion even at high temperatures that is an attraction for elevated temperature application is a challenge to achieving equilibration and requires extended (100 – 400 hour) high temperature annealing. In addition, EPMA determination of the co-existing phase compositions requires special care to obtain reliable boron measurements [00FOU]. As a result the initial phase diagram reported by Nowotny [57NOW] that was based upon relatively short time annealing has been modified in Figure 5 to reflect the reduced solubility of the binary phases in the ternary system.

As temperature increases from 1600 °C to 1950 °C, the Si and B solubility limits of Mo(ss) increase from 2.91 at%Si to 6.08 at%Si, and 0 at%B to 1.29 at%B, respectively. The Mo<sub>3</sub>Si phase has a limited homogeneity region that ranges from about 24 to 25 at. % Si and a negligible B solubility [00ROS]. The compositional boundary of Mo<sub>5</sub>Si<sub>3</sub> (T<sub>1</sub> phase) on the Mo-rich side extends to ~37 at% Si and on the Si-rich side to ~39 at% Si. The B solubility in the T<sub>1</sub> phase has been found to be much more limited than that reported by Nowotny [57NOW] and is

in agreement with a recent assessment [00HUE]. The Si solubility limit of MoB is negligible up to 1950°C. The Mo<sub>2</sub>B phase has negligible Si solubility at 1600 °C, but the solubility limit reaches 1.8 at.%Si at 1950°C.

The homogeneity range changes of the T<sub>2</sub> phase with increasing temperature are shown schematically in Figure 6. The stoichiometric composition is barely within the T<sub>2</sub> single-phase field. In the Mo(ss)-T<sub>2</sub>-Mo<sub>2</sub>B and the Mo(ss)-T<sub>2</sub>-Mo<sub>3</sub>Si three-phase equilibrium regions the T<sub>2</sub> boundary composition shifts towards the Mo(ss) solid solution phase with increasing temperature. Due to the larger size of a Mo atom compared to Si and B atoms, Mo concentrations in excess of stoichiometry most likely develop from metalloid constitutional vacancies as illustrated in Figure 6. In comparison in the MoB-T<sub>2</sub>-Mo<sub>5</sub>Si<sub>3</sub> three-phase equilibrium region, as temperature increases, the B solubility decreases and the Si solubility increases in the T<sub>2</sub> phase while the Mo solubility approximately remains constant reflecting the anti-site substitution between the Si and B sublattice sites.

#### 2.4. Phase Stability Relation to Processing

For the most part the current experience with Mo-Si-B alloys has been established with laboratory scale samples. For applications there are some processing issues that require resolution in order to achieve scaled up volumes. With the Mo-rich alloys of interest two main processing routes have been explored that are based upon ingot solidification and powder processing [99SCH]. With arc casting the as-solidified ingots tend to exhibit segregation and non-equilibrium boride phases that are difficult to remove by annealing or hot working. Initial efforts in powder processing of test samples were based upon the consolidation of atomized powders that provided a baseline of mechanical properties [97BER]. The scale up of the atomization approach is challenging due to the high temperature necessary and attempts to bypass this by using a rotating electrode method for powder generation encounter the difficulties noted for ingot solidification. Further effort is necessary to explore this route fully; especially for alloy compositions beyond the baseline ternary system. Another powder processing pathway based upon reaction synthesis of elemental powders has shown some promise. For example, Je'hanno et. al. have synthesized a triplex microstructure of Mo + Mo<sub>3</sub>Si + Mo<sub>5</sub>SiB<sub>2</sub> by ball milling of elemental powders and hot isostatic pressing to react the components [06JEH, 04JEH]. Following synthesis, the microstructure retained a sub micron phase size and moreover exhibited superplastic behavior at 1400°C. This observation indicates the possibility for fabricating final shapes by hot forging. However, before the fabricated components are used in service they must be annealed at high temperature (e.g. well above 1600°C) in order to coarsen the microstructure and enhance the creep resistance. In addition, in alloy powders that have been treated to develop an outer Mo layer before consolidation, the triplex microstructure morphology could be altered to yield a continuous Mo phase that can be useful for toughness enhancement [02SCH]. Besides the reaction synthesis of elemental powder compacts, a related approach based upon the reaction synthesis between elemental Mo and Si<sub>3</sub>N<sub>4</sub> and BN powders has been shown to yield the triplex microstructure [04COC]. With the powder synthesis methods, common concerns include the amount of residual porosity, the incorporation of inclusions (e.g. SiO<sub>2</sub>) as well as the large-scale uniformity of the microstructure. While the powder approaches address the solidification challenges in the baseline ternary system, the guidance from the current work has identified quaternary alloying additions that allow for bulk solidification without large scale segregation. With the limited work that has been pursued on processing it is evident that there



are real challenges to obtaining scaled up volumes that exhibit a consistent performance. Both of the main processing routes have difficulties, but there has also been progress that warrants further work with the guidance of the foundation of phase stability relations.

## 2.5. Thermodynamic Modeling in Mo-Si-B and Mo-TM-Si-B Systems

It is worthwhile to consider briefly some of the contemporary approaches to developing phase stability models in the complex multicomponent multiphase Mo-Si-B ternary system and Mo-TM-Si-B systems. In terms of thermodynamic modeling, the major challenge continues to be in the application of the CALPHAD approach which must evolve from a currently optimized two sub-lattice model [05YAN] to a four sub-lattice model to accommodate the complex defect structures present in Mo-Si-B system. The four sub-lattice thermodynamic model follows the four unique Wyckoff atomic positions within the  $T_2$  phase consistent with the two metal sites and two different metalloid sites given the fact that the crystal structure is highly ordered. Thus, further development of the experimental database on the constitutional defect structures at ultra-high temperature is important especially as they relate closely with the dislocation behaviors and overall high-temperature mechanical performances as well as the diffusion characteristics which in turn affect the environmental resistance. In this discussion the treatment is limited to cover only the CALPHAD modeling techniques and their application to represent the  $T_2$  phase both in the ternary and quaternary systems. Details on the optimized thermodynamic parameters are available in the references cited.

While there have been a few attempts to develop thermodynamic models for parts of the Mo-Si-B ternary system [05YAN, 99FAN, 01KIM] there is a more limited number of published thermodynamic models and optimized parameters of the ternary-based  $T_2$  phase [05YAN]. In fact, most of the reported thermodynamic models for even the binary -based  $T_2$  phases are based on treating the  $T_2$  phase as a line compound [02FER]. The only thermodynamic model to incorporate some of the defect structures has been the two sub-lattice model in the Mo-Si-B system developed by Yang et. al. [05YAN] based on the experimental database primarily from the 1600°C ternary phase diagram, precipitation reactions [99SAK] and the liquidus projections [01KIM, 01PER, 00NUN, 02KAT]. The model uses two sub-lattices; with one sub-lattice for the metal sites and the other sub-lattice for the metalloid sites. This implies that the model assumes that there is no distinction between the Si and B sites i.e a continuous solid solution of hypothetical compounds of  $Mo_5Si_3$  and  $Mo_5B_3$  with the  $T_2$  crystal structure. To represent the observed Mo precipitation in the  $T_2$  phase upon annealing, the model applies metalloid vacancies that yield an apparent excess Mo, i.e with the introduction of a hypothetical compound of  $(Mo)_5(Va)_3$  – a  $T_2$  phase with Mo atoms filling in the metal sites and the vacancies in all metalloid sites. Thus, the  $T_2$  phase is represented by an 'area' of a triangle of end points;  $(Mo)_5(Va)_3$ -  $Mo_5Si_3$ -  $Mo_5B_3$  as shown in Figure 7a. The thermodynamic model has been successful in representing the topology of the liquidus projection in general and the observed tendency of B-rich compositions for 'anti-site' substitution. The model has been also used to represent the phase relations in the quaternary system of Mo-Ti-Si-B with a solid solution extension of the (Mo,Ti) metal sites [05YAN]. In the quaternary  $T_2$  phase model, the vacancy defect was apparently dropped so that the  $T_2$  phase in the quaternary system is represented by a 'rectangular' slice of the end points;  $Mo_5Si_3$ - $Mo_5B_3$ - $Ti_5Si_3$ - $Ti_5B_3$  (Figure 7b) with their interaction parameters. These approaches have been adequate to show the general phase relations although due to

the limited data available on the solidification reactions in the quaternary systems, a more complete database is definitely needed to yield more reliable thermodynamic parameters. Furthermore, the presence of defect structures aside from the (B,Si) anti-site substitution can not be modeled by the two sub-lattice approach due to the limited area it represents. For this, a more complete thermodynamic database on the BCC precipitation reactions in Mo-Ti-Si-B system is needed for example so that constitutional vacancies can be modeled adequately. Indeed, a complete thermodynamic representation of the  $T_2$  phase in the ternary system must also take into consideration the highly ordered nature of the metalloid sites with their own corresponding sub-lattice at the minimum. Additionally, as indicated in the experimentally determined Mo-Si-B 1600°C isothermal section, there must be additional constitutional defect structures introduced to represent the 'Mo-poor' and 'B-rich' region of the  $T_2$  phase. This can not be modeled by the two sub-lattice model due to the inadequacy to extend the Mo compositions below 62.5 at. %.

For the quaternary system, one must also consider the fact that there are two distinctly different Mo sites in the  $T_2$  phase i.e the 'center' Mo site and the 'corner' Mo site with completely different geometric and electronic structure characteristics. Thus, the preferences for transition metal substitution for the two sites are not necessarily equivalent. In fact, recent work on the  $T_1$  phase for example [03FU, 05RAW], which has also two distinct Mo sites like the  $T_2$  phase, shows that the difference in the site preference can be quite large and in turns affects important physical properties such as the degree of thermal expansion anisotropy.

## 2.6. Kinetic Behavior in the $T_2$ Phase

To investigate the diffusion kinetics in the  $T_2$  phase, a  $\text{Mo}_2\text{B}/\text{Mo}_5\text{Si}_3$  diffusion couple has been used for determining the diffusion coefficients [06KIM]. In the  $\text{Mo}_2\text{B}/\text{Mo}_5\text{Si}_3$  diffusion couple annealed at 1600 °C the initial transient pathway that develops due to sluggish kinetics evolves into a steady state diffusion pathway of  $\text{Mo}_2\text{B}/T_2/\text{Mo}_5\text{Si}_3$  after long term (i.e. 400 hours) annealing as indicated in Figure 8a. Based on the analysis method developed by Dayananda [96DAY], the interdiffusion coefficients have been determined from the diffusion couple experiments and the composition profiles such as that shown in Figure 8b. The four independent average interdiffusion coefficients that were determined to represent diffusion in the  $T_2$  phase were of the order of  $10^{-15} \text{ m}^2/\text{s}$  at 1600°C and indicate that the Si and B diffusion behaviors are mainly controlled by the Si concentration gradient. A sluggish diffusion in the  $T_2$  phase was also observed in the analysis of vapor-solid diffusion experiments [06DHE].

In order to compare the diffusion behavior of the  $T_2$  phase with that observed for the  $\text{Mo}_5\text{Si}_3$  phase, the integrated interdiffusion coefficients for the  $T_2$  phase have been determined. The integrated interdiffusion coefficient of Si,  $\tilde{D}_{\text{Si},\Delta C}^{\text{int}}$ , is introduced which relates the interdiffusion coefficient to the interdiffusion flux for phases with a limited homogeneity range [96DAY, 99DAY]:

$$\tilde{D}_{\text{Si},\Delta C}^{\text{int}} = \overline{\tilde{D}_{\text{Si}}(T_2)} \Delta C_{\text{Si}} = \int_{x_1}^{x_2} \tilde{J}_{\text{Si}}(x) dx \quad (1)$$

where  $x_1$  and  $x_2$  are the relative distances from an arbitrary plane of reference, corresponding to boundary compositions of a  $T_2$  phase composition range in the concentration profiles, and  $\tilde{J}_{\text{Si}}(x)$  is the interdiffusion flux,



$\Delta C_{Si}$  is difference between the Si concentrations at  $x = x_2$  and  $x = x_1$ , and  $\overline{\tilde{D}_{Si}}(T_2)$  represents the average effective interdiffusion coefficient of Si over the  $T_2$  phase composition range. The integrated interdiffusion coefficients of B, Si and Mo in the  $T_2$  phase at 1600 °C are  $1.3 \times 10^{-13}$  cm<sup>2</sup>/s,  $-1.7 \times 10^{-13}$  cm<sup>2</sup>/s and  $3.5 \times 10^{-14}$  cm<sup>2</sup>/s. The activation energies for Mo, Si and B integrated interdiffusions are 439 kJ/mol, 355 kJ/mol and 338 kJ/mol, respectively. Tortorici et al. [99TOR] found the activation energy for integrated interdiffusion in MoSi<sub>2</sub> to be  $130 \pm 20$  kJ/mol and that for Mo<sub>5</sub>Si<sub>3</sub> to be  $210 \pm 10$  kJ/mol in the Mo/Si diffusion couples annealed at 900 – 1350 °C. Their estimated integrated interdiffusion coefficient for the Mo<sub>5</sub>Si<sub>3</sub> phase was  $2.3 - 2.6 \times 10^{-11}$  cm<sup>2</sup>/s at 1350 °C. Based on the integrated interdiffusion coefficients at different temperatures, the prefactor was estimated at  $1.3 \times 10^{-4}$  cm<sup>2</sup>/s so that the integrated interdiffusion coefficient at 1600 °C was evaluated to be  $1.8 \times 10^{-10}$  cm<sup>2</sup>/s. Ito et al. [04ITO] examined the evolution kinetics of Mo<sub>5</sub>Si<sub>3</sub> in the MoSi<sub>2</sub>/Mo(ss)+Mo<sub>5</sub>SiB<sub>2</sub> diffusion couples that were annealed in ranges of 1300 – 1500 °C. The prefactor was determined to be  $1.2 \times 10^{-3}$  cm<sup>2</sup>/s and the activation energy for integrated interdiffusion in Mo<sub>5</sub>Si<sub>3</sub> was estimated at 240 kJ/mol. The evaluated integrated interdiffusion coefficient at 1600 °C was  $2.4 \times 10^{-10}$  cm<sup>2</sup>/s. Hayashi et al. [05HAY] recently estimated the activation energy for integrated interdiffusion of Mo<sub>5</sub>Si<sub>3</sub> in the MoSi<sub>2</sub>/T<sub>2</sub> diffusion couple at about 300 kJ/mol, and the integrated interdiffusion coefficient for Mo<sub>5</sub>Si<sub>3</sub> was  $3.1 \times 10^{-10}$  cm<sup>2</sup>/s at 1600 °C. The measurements reveal that the integrated interdiffusion coefficient of Si in the  $T_2$  phase is smaller by about three orders of magnitude than that for the Mo<sub>5</sub>Si<sub>3</sub> phase. The activation energies for integrated interdiffusion of Si for the  $T_2$  phase is 355 kJ/mol that is larger by 56 kJ/mol than that [05HAY] for the Mo<sub>5</sub>Si<sub>3</sub> phase. The  $10^3$  difference between the integrated interdiffusion coefficients of Si for the  $T_2$  and Mo<sub>5</sub>Si<sub>3</sub> phases appears to mainly originate from differences in the activation energy,  $\Delta Q$  between the  $T_2$  and Mo<sub>5</sub>Si<sub>3</sub> phases because  $\exp(-\Delta Q/RT) = 2.7 \times 10^{-2}$  at 1600°C. However, the influence of a reduced correlation factor in a non cubic ordered structure with anisotropic diffusion can also contribute to the reduced diffusivity and should be considered in further study.

## 2.7. Annealing Response of Constitutional Vacancies and Dislocations in the $T_2$ phase

The ternary Mo<sub>5</sub>SiB<sub>2</sub> ( $T_2$ ) phase is the key constituent in the Mo-Si-B ternary system [06KIM, 00NUN, 97NUN] and exhibits a distinct range of homogeneity around the stoichiometric composition. The constitutional vacancy has been proposed as a defect mechanism to explain the dependence of the lattice parameters on the  $T_2$  phase composition [97NUN]. The  $T_2$  phase has also been found to exhibit a temperature dependent solubility, which is manifested by the Mo(ss) precipitation reaction in the Mo(ss)/ $T_2$  two-phase alloys upon annealing [99SAK, 97NUN]. Moreover, small Nb additions to a Mo(ss)/ $T_2$  two-phase alloy inhibit the formation of Mo(ss) precipitates in  $T_2$  phase. Thus, the stability of  $T_2$  phase is strongly related to constitutional defects [05SEK].

As depicted in Figure 9, the as-cast microstructure of a Mo-10Si-20B alloy consists of three phases: Mo(ss), Mo<sub>5</sub>Si, and  $T_2$ . The primary solidification phase is a faceted  $T_2$  phase, and the Mo(ss)/ $T_2$  mono-variant eutectic products have formed to enclose the  $T_2$  primary, followed by the formation of Mo(ss)/ $T_2$ /Mo<sub>5</sub>Si three-phase microstructure as the final solidification product. After the annealing of the alloy at 1600 °C for 150 hours, Mo(ss) particles have precipitated in the primary  $T_2$  matrix. TEM observations have revealed that the dislocation density in

the primary  $T_2$  phase increases with annealing time. Few dislocations and no precipitates are present in the  $T_2$  primary of an as-cast alloy, while many dislocations have developed in the  $T_2$  phase of the alloy annealed at 1550 °C for 20 hours. At the same time, it is also evident that the plate shaped Mo(ss) particles have preferentially precipitated on these dislocations. Considering that these dislocations have developed only by annealing, and the homogeneity range of the  $T_2$  phase is attributed to the introduction of constitutional defects [97NUN], the dislocations are formed by the removal of excess constitutional vacancies during annealing. This result is supported by the lattice parameter variation with annealing time. The volume of the  $T_2$  unit cell increases with annealing time, although larger sized excess Mo atoms are eliminated to form the Mo(ss) precipitates during annealing. Consequently, the excess vacancies retained from high temperature in  $T_2$  phase are removed to form dislocations upon annealing, which then provide the heterogeneous nucleation sites for the subsequent (Mo) precipitation.

The extensive development of edge dislocations supports the fact that the dislocations formed in  $T_2$  phase of annealed alloys are caused by the vacancy annihilation process. When the excess vacancies are attracted and collapsed into dislocations, the excess vacancy concentration,  $\Delta C_v$  is given by:

$$\Delta C_v = 0.5\rho b \quad (2)$$

where  $\rho$  is the dislocation density,  $r$  is the average radius of the dislocation loops, and  $b$  is the magnitude of the Burgers vector. The dislocation densities in the  $T_2$  phase of the annealed Mo-10Si-20B and Mo-13Si-28B alloys were determined as  $3 \times 10^{-13} \text{ m}^{-2}$  and  $1 \times 10^{-13} \text{ m}^{-2}$ , respectively. These dislocation densities correspond to excess vacancy concentrations estimated as  $0.9 \times 10^{-2}$  and  $0.3 \times 10^{-2}$ , respectively, under the assumptions that the average radius of the dislocation loops is 1  $\mu\text{m}$ , and the Burgers vector of dislocation is 0.601 nm ( $b = \langle 100 \rangle$ ). When the presence of the thermal vacancies and anti-site defects is ignored, the constitutional vacancy concentration in a  $T_2$  phase with a Mo-rich composition can be estimated from the Mo content as follows:

$$C_v = 1 - 5/(8C_{\text{Mo}}) \quad (3)$$

where  $C_v$  is the total constitutional vacancy concentration on the Si and B sites, and  $C_{\text{Mo}}$  is the Mo content in the  $T_2$  phase [06K1M]. The Mo concentrations of the  $T_2$  phase at the Mo/ $T_2$  two phase region has been measured as 0.637 at 1600 °C, and as 0.643 at 1870 °C [06JEH]. Thus, the calculated constitutional vacancy concentrations are: 1.9 % at 1600 °C, and 2.8 % at 1870 °C. The agreement with the vacancy content estimated from the loop density indicates that many of the excess vacancies have aggregated into dislocation loops. While there is a consistent understanding of the role of constitutional defects in the development of dislocation loops and precipitation, the role of the dislocation loops in the deformation behavior is an open issue. Similarly, other defects such as the presence of stacking faults within  $T_2$  phases as shown in the TEM examination (Figure 10) require further examination to determine their influence on the phase stability.

The dislocations have been analyzed by the thickness fringe method [80ISH], which can uniquely determine the Burgers vectors by counting the number of thickness fringes terminated at the end of each dislocation imaged in weak-beam mode under three different reflection vectors. The dislocation networks formed in the  $T_2$  phase of Mo-10Si-20B and Mo-13Si-28B alloys mainly consist of edge dislocations. Most of the dislocations formed in  $T_2$  phase of the former alloy have the Burgers vectors of  $\langle 100 \rangle$ , and  $\langle 110 \rangle$  as shown in Figure 11, while the dislocations with the Burgers vectors of  $\langle 100 \rangle$  and  $1/2\langle 111 \rangle$  are typically observed in the latter alloy. Field et al.

have examined possible slip systems in  $T_2$  phase based on the crystallography and energetic factors, and found that two slip system,  $\langle 100 \rangle / \{001\}$  and  $1/2 \langle 111 \rangle / \{112\}$  are favored over other slip systems [01FIE]. These two slip directions are consistent with the two smallest lattice translation vectors in the  $T_2$  crystal, and would be reasonable from an elastic energy point of view. The dislocation line energy is estimated by  $E = Kb^2$  where  $K$  is an energy factor which is a function of the elastic constants and the dislocation direction [97BER, 06JEH]. However, during annealing of the  $T_2$  phase many  $\langle 110 \rangle$  dislocations with energies that are about twice as large as those of  $\langle 100 \rangle$  dislocations developed by vacancy agglomeration. Thus, an analysis based solely on elastic energy is insufficient.

The dislocation analysis studies reported to date have demonstrated that the slip systems in  $Mo_5SiB_2$  strongly depend on the deformation and composition, which makes it difficult to understand the intrinsic nature of dislocations based only on simple elastic energy considerations. Moreover, it is clear that the structure and mobility of dislocations are determined by the interatomic interactions and may be understood on the microscopic quantum mechanical level. For example, *ab initio* methods have been successfully used for the calculations of stacking faults, grain boundaries, dislocation-impurity interaction, etc., and provided information for an analysis of the deformation behavior. The large progress is achieved with the use of generalized stacking fault energies [74VIT], which represent the shear energies for the planar fault and allows one to simulate the dislocation core structure and Peierls stress within the Peierls-Nabarro (PN) model. Such an approach was successfully used to study the dislocation structure in a number of materials and helped to establish the intrinsic mechanism of many aspects of deformation behavior including the brittle-ductile transition and solid solution softening, [02WOO;05TRI].

To predict the possible slip system and analyze the fracture and deformation mechanisms for the  $T_2$  phase we have collaborated with Professor A. Freeman who has performed *ab-initio* calculations of generalized stacking fault (GSF) energies for some directions on the  $\{001\}$  and  $\{010\}$  planes. Besides the GSF energies which describe the planar shift, we also calculated the energies of atomic row displacements, when only an atomic line is shifted.

From the first principles calculations the generalized stacking fault energies were analyzed for some directions on  $\{001\}$  and  $\{010\}$  planes. A striking result was obtained that sliding for  $\langle 100 \rangle \{001\}$ ,  $\langle 110 \rangle \{001\}$  and  $\langle 001 \rangle \{010\}$  directions is characterized by close values of the unstable and stable stacking fault energies. From this result it is evident that minor differences in applied deformation and composition may account for the variety of reported dislocation types. The shortest Burgers vector of the full dislocation corresponds to  $\langle 100 \rangle (100)$ , so that this slip should be slightly preferable among non-dissociated dislocations. We found various types of stacking faults on the  $\{001\}$  and  $\{010\}$  planes and predict the possibility of splitting into two and three partials with separation larger than 4.5 nm for the edge  $\langle 100 \rangle \{001\}$  and  $\langle 110 \rangle \{001\}$ ,  $\langle 001 \rangle \{010\}$  dislocations, with the collinear Burgers vectors of  $b = a/2$ ,  $b = \sqrt{2}/3$  and  $b = c/4$ ,  $c/2$ ,  $c/4$ , respectively. The analysis of dissociated dislocations does not show a strong preference for a slip system, though the simulation of dislocation by the line defects points out that the atomic  $\langle 001 \rangle \{010\}$  displacement has the lowest line energy among possible perfect dislocations.

Thus, the inclusion of the bonding energetics provides important new insight on the dislocation and deformation behavior in the  $T_2$  phase. At the same time the first principles calculations indicate that several slip systems have relatively close energies that suggests with suitable alloying it may be possible to promote operation of



multiple systems that can benefit low temperature ductility. Further work and continued collaboration with Professor Freeman in this promising area and others will be very valuable.

## 2.8. Alloying behavior in $T_2$ Phase

In order to develop the understanding of phase stability in the baseline ternary system and to provide a database for the assessment of the geometric and electronic structure contributions to phase stability, a systematic study was conducted on the alloying behavior of the  $T_2$  phase. All of the refractory metal additions from the Group IV, V and VIB metals that were examined show a large degree of substitutional alloying in the  $T_2$  phase and a more limited alloying extent in other silicide structures. In the case of V, Nb, Cr and W substitutions, there is a continuous solid solution in the  $T_2$  phase based on the samples that were annealed at  $1600^\circ\text{C}^{63,79}$ . In the case of Group IVB metal additions, Ti and Hf do not form a complete solid solution in the  $T_2$  phase, however in each case, an extended solubility was observed such that Ti-rich and Hf-rich  $T_2$  phases can be stabilized (i.e. replacement of Mo content exceeds 50 at. %) as shown in Figure 12. This implies that the stability of  $T_2$  phase in the quaternary Mo-Ti/Hf-Si-B extends deeply into the Ti/Hf-rich side. In all cases, the total concentration of the metal components remains close to the stoichiometric value (62.5 at. %), indicating that the refractory metal substitutions strictly replace the Mo atoms at the metal sites in the crystal structure. The extended solubility in the  $T_2$  phase that mimics the alloying behavior in the BCC phase is not necessarily typical of other Mo-rich boride or silicide phases. For example, the  $\text{Mo}_3\text{Si}$  A15 phase has a very limited solubility for W or Nb [00MA]. The  $T_1$  phase has an extended solubility with Group VB metals, but a more limited solubility for the Group IVB metals. This is primarily due to the fact that metals such as Hf and Zr tend to stabilize hexagonal based silicides such as the  $D8_8$  phase. Similarly, while there is a continuous solid solution with Nb for the  $\text{Mo}_2\text{B}$  phase, there is a little solubility of Ti or Hf in  $\text{Mo}_2\text{B}$  [80ZAK]. Figure 13 sums up the extended alloying behavior of  $\text{Mo}_5\text{SiB}_2$  into four categories. The first one is the continuous solid solution with Nb to replace Mo which accompanies with the shift of the metalloid proportion (i.e Si/B) to the Si-rich side (Figure 13a). The second type is the continuous substitution of Mo by Cr (Figure 13b). The substitution is followed by the shift in the metalloid content to the B side. In the case of alloying elements like V or Ti, the substitution does not appear to affect the composition of the metalloids in a significant way and continues either to the other end of the ternary side (Figure 13c) or deep within the quaternary system of Mo-TM-Si-B system (Figure 13d).

In contrast to the extended alloying solubility of the Group IV, V and VIB metals, elements in Group VIIB and VIII show a very limited substitutional alloying in the  $T_2$  phase [03SAK]. The limited solubility of nickel to substitute for Mo may be explained in part from the size effect (the difference in atomic radius is more than 10 %). However, the low solubility of rhenium in the  $T_2$  phase as shown in Figure 14 could not be simply argued from the a geometrical point of view. The atomic radius of rhenium differs from that of molybdenum by no more than 2 %. In order to understand the fundamental basis of the observed alloying behavior it is necessary to examine more closely the structural arrangements in the intermetallic phases to elucidate the local environment of the refractory metal that will also impact the governing bonding arrangements.

## 2.9. Evaluation of Phase Stability

In general, the size factor metrics such as the atomic radius of the metal components or the atomic radius ratio of metal to metalloid atoms have been shown to play an essential role in alloying behavior as exemplified by the Hume-Rothery 15 % rule [83WIL]. Similarly, the effect of chemical bonding within the structure as expressed by parameters such as valence electron concentration per atom ( $e/a$ ) has been shown to be essential in combination with the size factors to define the phase stability. In particular, it has been shown previously that the  $e/a$  criteria can be successfully applied to transition metals and transition metal-based compounds [85FU, 83OHN, 87XU, 89XU, 90XU]. Moreover, the  $e/a$  criteria can also be correlated directly to some of the characteristics in the electronic structure of the compounds that favor a high cohesive energy [89BOE]. For example, for a stable and high melting transition metal based BCC phase, the favorable  $e/a$  values range between 5.0 (corresponding to that of Group VB metals such as Nb) and 6.0 (corresponding to that of Group VIB metals such as Mo) with the highest cohesive energy (at the ground state) corresponding to an  $e/a$  of 5.5 [83WIL, 89HAR, 77PET]. The optimum  $e/a$  value and the maximum cohesive energy are characterized by the BCC phase electronic structure with all of the bonding states filled and none of the high energy anti-bonding states are occupied. Furthermore, the extent of solid solution among the transition metals can also be estimated from a similar analysis [83WIL, 89HAR, 77PET].

While there have been numerous studies of the alloying behavior in BCC refractory metals, the analysis of the alloying behavior in refractory metal silicide phases is relatively limited. In multiphase designs an understanding of the relative solubility of a given addition in each of the coexisting phases is essential to judge how the solute addition is partitioned between phases and the influence of the solute addition on the phase boundaries and relative phase stability. Since the refractory metal intermetallic phases often display variable and asymmetrical homogeneity ranges about the stoichiometric composition, the analysis of alloying behavior requires an examination of the local atomic environment in order to evaluate the key geometric and electronic interactions that control the stability.

In order to address this long standing challenge some contemporary approaches have been effective in modeling phase stability in complex multicomponent, multiphase systems. For example, electronic structure calculations have been advanced by the use of density-functional theory (DFT) as a many-body approach along with the application of the local density approximation (LDA) and gradient-dependent approximation (GDA). By simplifying the DFT problem to treat valence electrons under the assumption that the core electrons experience little change due to the chemical reactions, further advancement has been achieved by the introduction of the plane-wave pseudopotential (PW-PP) techniques. This approach has enabled the band structures as well as other physical properties of the transition metals, in particular, to be elucidated. Additionally, the applicability of the theoretical approach of the 'rigid band model' to elucidate the relative phase stability of many transition-metal based intermetallics has been well-documented [85FU, 89BOE, 89HAR].

In the present discussion, a similar approach to phase stability analysis in terms of the electronic structure and the level of bonding states occupancy is examined by means of a number of available and well-known ab-initio codes [84SKR]. Based on the calculated electronic structure, the criteria for the optimum  $e/a$  and the transition metal alloying trends are estimated and compared with that calculated for the BCC phase. For intermetallic phases the initial analysis is based upon stoichiometric compositions. An important compliment to phase stability analysis relates to the constitutional defect structure that governs the extent of departure from stoichiometry and homogeneity

range. In addition to the computational analysis of stability, the predicted behavior has been evaluated by experimentally determining selected alloying behavior in order to establish guidelines for the stability in the silicide phases for a wide range of potential alloying elements.

## 2.10. Structural Stability of the $T_2$ Phase

The  $T_2$  phase is one of the most common "5-3" metal-metalloid compounds found in the large array of metal-based systems spanning from the Alkaline-earth metal to the Late Transition Metals. In fact, one can plot the occurrence of this type of crystal structure based on the metal or metalloid elements used on the majority of the elements in the periodic table as shown in Figure 15 with a varying combination of metal-metalloid pairings which seem to highlight the role of atomic radius ratio. For example Alkaline-earth or Lanthanide-based  $T_2$  phases exist when the metal is paired with metalloids with a relatively large atomic size such as Si, Sn or Ge, whereas the transition metal-based  $T_2$  can be stabilized with metalloid pairs of smaller atomic sizes such as boron.

### 2.10.1 Geometric Factors

In general, atomic size is a key underlying factor in determining metalloid solubility in refractory metal silicides. There is typically a strict range of atomic size ratio of metal to metalloid that is favorable for the structural stability [60PAU]. The  $T_2$  structure has the highest volume packing density among known  $TM_5X_3$  compounds ( $TM \equiv$  Transition Metal,  $X \equiv$  Metalloid) [57NOW, 58ARO, 59ARO, 57NOW, 60NOW]. This suggests that the stability is governed by the drive to achieve a high packing density of the metal and metalloid constituents. A manifestation of the size factor is evident in the restriction of the  $c/a$  range of all known  $T_2$  phases as shown in Figure 16. Furthermore, there is a general correlation between the radius ratio of the metal to metalloid atoms and the  $c/a$ . A systematic analysis on the change of  $c/a$  with a substitution of Mo (0.13 nm) by larger size atoms (such as Ti with atomic radius  $r_M = 0.16$  nm) clearly shows the consistent trend of an increase in  $c/a$  with a corresponding increase in the atomic radius ratio between the transition metal and the metalloid ( $r_M/r_X$ ). With an increase in the atomic radius ratio between metal to metalloid, there is a corresponding increase the aspect ratio ( $c/a$ ) of the tetragonal crystal structure in order to minimize the interstitial volume [01PER].

The geometric rule however does not address the fact that there is an unusually large solubility of the refractory metals in the Mo sites even with elements such as Hf or Ti for which the respective RM-Si-B ternary system exhibits a stable  $D8_8$  phase. In fact, the alloying behavior is apparently quite comparable to the alloying behavior of RM substitutions in the Mo BCC phase. The similarity in the alloying between the metal sites in the  $T_2$  and BCC ( $A2$ ) phases may be traced to the fact that similar to the BCC crystal structure, the  $T_2$  structure also maintains a relatively high coordination number (CN) of metal-metal atomic contacts to retain a relatively close-packed structure [58ARO, 59ARO]. Furthermore, the  $T_2$  crystal structure ( $I4/mcm$ ) retains a body-centered symmetry for the refractory metals as exemplified by the similar atomic surroundings of Mo atoms at the (0,0,0) and ( $\frac{1}{2}$ ,  $\frac{1}{2}$ ,  $\frac{1}{2}$ ) positions in the lattice. The BCC-like environment is quite evident by examining the surroundings of the Mo atomic sites as depicted in the Figure 17. The figure shows that the CN of Mo-center and Mo-edge contacts in the Mo clusters in the  $T_2$  crystal structure is actually eight which is the same as that of the BCC lattice. In fact, the



$T_2$  structure can be viewed as constructed from vertical chains of the BCC-like corner-sharing Mo clusters connected by the anti-prismatic hole filled by Si. Examination of the inter-atomic distances further supports the resemblance [01RAW]. The Mo-Mo interatomic distances associated the nearest neighbors are close to those in the BCC lattice as well. The shortest Mo-Mo interatomic distance yields a value of 0.2737 nm (at room temperature) which is similar to that of the Mo-Mo interatomic distance in the BCC lattice (0.272 nm).

The presence of the BCC-like characteristics for the metal component can be traced back to the fact that the "A-A" layered stacking is stabilized only in the  $T_2$  phase (in comparison to the other silicides as well as borides). Both the  $Mo_2B$  and  $Mo_5Si_3$  phases stabilize only the A- A  $1/2/1/2$  atomic stacking. From the perspective of atomic clusters within the crystal structures, due to the symmetry associated with the A- A  $1/2/1/2$  atomic stacking, the crystal structures for both phases are dominated by the Mo-Si and Mo-B clusters and the BCC-like environment is absent. While there is Mo-Mo contact within the structures, the Mo-Mo interatomic distance is not similar to that in the BCC phase. Instead, there is a characteristic of a very short interatomic Mo-Mo distance within the crystal structures as depicted in Figure 2 and 3. The interatomic distance of Mo-Mo in the  $T_1$  phase is 0.245 nm whereas the shortest interatomic Mo-Mo distance in the  $Mo_2B$  phase is 0.267 nm. Indeed, the consequence of the BCC-like environment in the  $T_2$  phase can be directly linked to the solubility behavior (in comparison to that of  $Mo_2B$  and  $Mo_5Si_3$  phases) and the electronic factors such as the  $e/a$  ratio.

#### 2.10.2. Electronic Factors in Phase Stability

The capability of Group IVB elements to substitute for Mo in  $Mo_5SiB_2$  is unusually large considering the fact that the  $T_2$  phase is not stabilized in the respective TM-Si-B systems and the atomic size difference between Mo and these metals is relatively large. The extended solubility exceeds the level that would be expected based upon the geometrical Hume-Rothery 15 % limit. For example, the atomic size of Hf is about 20 % larger than Mo, but the solubility is more than 50 at. %. On the other hand, Re has a limited solubility in  $T_2$  phase despite a mere 1-2 % difference in atomic size. Therefore, the electronic factors including the valence electron per atom ( $ve/a$ ) value and the density of states (DOS) must also be evaluated to elucidate the alloying behavior in the borosilicide  $T_2$  phase.

There have been limited studies on the relationship between alloying behavior and the electronic structure of metal rich silicides and borosilicides [99FU, 00FU]. The most recent work has been concentrated mostly on the effect of alloying on the physical properties such as thermal expansion and elastic moduli. In contrast, there have been several phase stability studies that focused on the rare earth (RE) and alkaline-earth (AE) based  $T_2$  phases such as  $La_5Si_3$  and  $Ca_5Ge_3$  where the phase stability criteria may not be similar to that of the transition-metal based  $T_2$  phase. The RE and AE - based  $T_2$  phases can be distinguished from the transition-metal based  $T_2$  phase by the value of the valence electron per atom ( $e/a$ ). A plot of occurrences of the known  $T_2$  compounds versus the  $e/a$  value is shown in Figure 18. Clearly, there are distinct groupings for the  $T_2$  phase. The low  $e/a$  range ( $e/a$  of 2-3)  $T_2$  phase occurs with the metal constituent as a rare-earth or alkaline earth metal and the high  $e/a$  range  $T_2$  phase ( $e/a$  of 4-5) occurs with a transition metal as the metal atom constituent. It is noteworthy that  $Mo_5SiB_2$  ( $e/a$  value 5.0) is positioned at the high end of the  $e/a$  range.

Combined criteria that include geometry and electronic factors to define the stability of the  $T_2$  phase are developed in Figure 19a that presents plots of the  $(e/a)$  versus the atomic radius ratio between the metal ( $r_M$ ) to metalloid/simple metal ( $r_X$ ) constituent of the  $T_2$  crystal structure. The two domains of  $T_2$  phase can clearly be discerned. More importantly, there are characteristics defining the two groups of  $T_2$  phase. Namely, the low  $e/a$   $T_2$  phase generally has a larger atomic radius ratio in comparison to that for the high  $e/a$   $T_2$  phases. The larger lattice unit is directly correlated to the fact that the metal constituent of the low  $e/a$   $T_2$  phase is composed of either rare-earth or alkaline earth metals which have a larger atomic radius than that for the transition metals. This further asserts a correlation between the volumes of the  $T_2$  unit cell with the size of the metal atoms. The relatively high value of the atomic radius ratio of low  $e/a$   $T_2$  phases has another important geometric characteristic. An evaluation of the packing efficiency of the  $T_2$  phase shows that the low  $e/a$   $T_2$  phase also has a much higher volume density per unit cell than that of low  $e/a$   $T_2$  phases (see Figure 19b). Thus, there is a general tendency for the low  $e/a$  value  $T_2$  phases to achieve a relatively high packing efficiency and consequently high atomic radius ratio. One possible explanation of the differences in the relative packing density of the two domains of  $T_2$  phases may be related to the nature of the bonding within the crystal structure, particularly between the metal constituents. In the progression from the rare-earth type of  $T_2$  phase to the transition metal type of  $T_2$  phase, there is an increasing dominance of stronger transition metal-metal bonding due to occupancy of the d electrons. The increasing dependency of the phase stability in the  $T_2$  phase to the directional metal-metal contact appears to limit the degree of packing efficiency of the transition metal-based  $T_2$  phase as indicated in Figure 19b. While the packing efficiency of the transition-metal-based  $T_2$  phase remains above 70 %, the value for the rare-earth and alkaline-earth-based  $T_2$  phases is even higher.

The  $e/a$  criterion can be directly related to the electronic structure of the  $T_2$  phase similar to the case of intermetallies in general [83WIL, 89HAR, 77PET, 97ZHU]. It has been established that a thorough separation between bonding and anti-bonding regions is characteristic of covalency and high cohesive stability. An 'optimal'  $e/a$  would therefore refer to the value of  $e/a$  that favors the complete filling of the bonding states [77PET]. An optimal  $e/a$  would therefore bring the highest occupied states (Fermi energy level) of the crystal structure to the position that separates the bonding and anti-bonding states. A low density of states at the Fermi level is favorable for the phase stability. The stability of the BCC phase is favorable with the  $e/a$  ratio values between 5-6 (the minimum gap in DOS corresponds to an  $e/a$  value of 5.5) [77PET]. Indeed, for a full phase stability analysis, the role of the vibrational and configurational entropy must also be taken into account and hence the absence of these factors represents one of the major limitations in the analysis developed from the ab-initio calculations at the ground state. However, as has been shown in a wide variety of transition-metal based intermetallies such as silicides, carbides and aluminides [85FU, 83OHN, 87XU, 89XU, 90XU], the most stable and highest melting temperature crystal structures tend to exhibit a minimum gap in their total DOS and that the position of the Fermi energy level (which constitutes the highest occupied energy states at the ground state) is very close to the minimum gap. Following this basis, an analysis on the position of the minimum gap within the total DOS has been performed for the  $T_2$  phase.

The calculated results of the DOS are plotted in Figure 20 for Mo-BCC,  $Mo_2B$  ( $CuAl_2$  – prototype),  $T_2$  and  $D8_8$  phases. The calculated total DOS for the BCC phase correctly reveals a minimum gap corresponding to an  $e/a$  value of 5.5 as has been previously reported [77PET]. In comparison, the  $e/a$  value for the  $T_2$  phase based on the

contribution from the transition metal constituents is 5.2 which is relatively lower. Thus, strictly from this line of analysis, there will be a greater likelihood for the  $T_2$  phase to be alloyed by particularly by Group IV metals than that of BCC Mo. In comparison to the  $T_2$  and BCC phases, the DOS for the  $D8_8$  phase shows the transition metal  $e/a$  value at the minimum gap of about 4, meaning that a stable  $D8_8$  phase will likely to have metal constituents that are composed of mostly Group IVB members. Indeed, the highest melting temperature  $D8_8$  phase is based on the Group IVB metals (Ti, Zr and Hf-based  $D8_8$ ) [00ZHA, 79KAU].

Based on a simple rigid-band approximation [87XU], the effect of alloying elements with a higher valence electron (VE) than Mo (such as rhenium) can first be approximated by simply adding the integrated area of the unoccupied states in the Density of States in the rigid band sense. Conversely, adding alloying elements with a lower valence electron concentration than Mo (such as titanium and niobium) will subtract a portion of the occupied states. From a more detailed evaluation of the Density of States of the  $Mo_5SiB_2$  [03SAK], it became clear that the energy position for the minimum gap for  $Mo_5SiB_2$  is lower than the Fermi level position of  $Mo_5SiB_2$ . Hence, from the perspective of the rigid band model, it is desirable to alloy  $Mo_5SiB_2$  with transition metals with a lower valence electron concentration (such as Group V and IVB metals) to bring the TM  $e/a$  value closer to the minimum gap position. On the other hand, the addition of a higher TM  $e/a$  ratio such as Re appears to be unfavorable energetically due to the fact that Re addition tends to favor an increased in the occupancy of the bonding states as confirmed by the results of the electronic structure (Figure 21). Indeed, the predicted low solubility of Re alloying to the Mo-based  $T_2$  phase is counterintuitive in light of the high solubility of Re in the Mo BCC phase and the fact that the atomic radius of Mo and Re is very close ( $r_{Re} = 0.197$  nm  $r_{Mo} = 0.201$  nm). However, this theoretical prediction along with the predicted large solubility of Ti and V in the  $T_2$  phase has been confirmed by the recent experimental studies (Figure 14) and indeed points the utility of electronic structure calculations in assisting the alloying design in Mo-Si-B system. Furthermore, the ab-initio analysis can be extended to higher order (multi-component) systems as exemplified in Figure 22 where the relative (in) stability of the  $T_2$  phase in the Mo-Ti-V-Si-B system can be quantitatively assessed using ab-initio-based quantitative metrics such as the degree of state occupancy beyond the 'minimum energy gap'.

Overall the computational tools have allowed us to probe new areas of phase stability in an informed systematic manner instead of the traditional inspired trial and error method. We have used the computational guidance successfully to employ selective alloy substitution to achieve new microstructures that offer new performance levels and multifunctional characteristics, but with this success it is now necessary to define the relevant phase reactions fully.

## 2.11 Multiphase Microstructure Design

A combined criteria of  $e/a$  and atomic size factor for the transition metals can be applied to design multiphase microstructures based on the extended two-phase field of BCC and  $T_2$ . The large extension of the solubility in TM with valence electron concentration to be equal or less than Mo in the  $T_2$  phase allows for the formation of new high temperature microstructures than are composed of BCC,  $T_2$  and additional phases to provide balanced properties. The general strategy for alloying design can be depicted in the schematics shown in Figure 23.



Near the Mo-Si portion of the ternary system of Mo-Si-B, there are two three-phase equilibria; BCC + T<sub>2</sub> + A15 and A15 + T<sub>2</sub> + T<sub>1</sub> phases. A number of new multi-phase equilibria that are based on the extended two-phase field of BCC + T<sub>2</sub> can be established by substituting Mo with the alloying elements. For example, by substituting Mo with Hf, a three-phase field of BCC + T<sub>2</sub> + D8<sub>8</sub> can be stabilized. On the other hand, substituting Mo with W or Nb stabilizes the BCC + T<sub>2</sub> + T<sub>1</sub> phases. The flexibility in modifying the structures of the multi-phase design is indeed the direct consequence of the relative similarity in alloying behavior of BCC and T<sub>2</sub> phases.

From the alloying strategy, new solidification microstructures of three-phase alloys be stabilized. For example, the three-phase combinations of BCC + T<sub>2</sub> + T<sub>1</sub> may be favorable relative to the BCC + T<sub>2</sub> + A15 since unlike the A15 phase, both T<sub>2</sub> and T<sub>1</sub> are creep and oxidation resistant particularly at high temperature. By means of Nb or W addition into Mo-Si-B alloys, a three phase BCC + T<sub>2</sub> + T<sub>1</sub> eutectic structure can be stabilized through the five-phase equilibrium due to the limited solubility of Nb or W in the Mo<sub>3</sub>Si (A15) phase [00SAK]:



which stabilizes a three-phase eutectic alloys of BCC + T<sub>2</sub> + T<sub>1</sub> (Figure 24). The stability of the two-phase field of BCC + T<sub>2</sub> can also be promoted by appropriate alloying in ternary systems where the two-phase field does not exist. For example, in the W-Si-B system, the T<sub>2</sub> phase does not form a two phase field with the BCC phase as shown in Figure 25. The primary reason is due to the fact that the competing boride (W<sub>2</sub>B) and silicide (W<sub>5</sub>Si<sub>3</sub>) phase are very stable. The W-based T<sub>2</sub> phase has a high VE of tungsten and the high Si content (the composition is non-stoichiometric and close to W<sub>5</sub>(Si,B)<sub>3</sub>). Furthermore, with the addition of rhenium into the BCC phase forming a ductile (Mo,Re) solid solution, a new three-phase alloy can be established composed of the T<sub>1</sub> and T<sub>2</sub> and the BCC phases. The intermetallic phases have a lower solubility in elements with higher VE than Mo (such as Re) due to the electronic factor and thus Re is highly partitioned to the BCC phase forming a BCC+T<sub>2</sub> + T<sub>1</sub> alloy ( Figure 26).

## 2.12. BCC + T<sub>2</sub> + T<sub>1</sub> Ultra-high Temperature Three-Phase Alloys

An important consequence of the new development in alloying strategy in the Mo-Si-B system is the ability to alter the phase constituents of the silicide phases used as the main source of silicon for oxidation protection. In the Mo-Si-B system, the Mo<sub>3</sub>Si (A15) silicide phase is in equilibrium with the BCC and the T<sub>2</sub> phase and serves as the primary source of Si within the alloy forming the three-phase field of BCC + A15 + T<sub>2</sub>. The three-phase combinations of BCC + T<sub>2</sub> + T<sub>1</sub>, which is not available in the Mo-Si-B system, is actually more favorable than the BCC + T<sub>2</sub> + A15 because unlike the A15 phase, the T<sub>1</sub> phase is creep and oxidation resistant phase particularly at high temperature [04ALU]. Further, there is an additional 'weight penalty' associated with the presence of a fairly Mo-rich silicides such as the A15 phase. In addition, the A15 phase is subject to phase transition even by a minor addition of alloying elements (e.g. Nb) due to the well-known intrinsic phonon-induced instability within the crystal structure [97SAD]. An examination of the 1600°C isothermal sections for the Mo-Si-B and Nb-Si-B systems in Figure 5 reveals the key features of the phase equilibria that provide essential guidance in achieving the desired microstructure. First, for refractory metal rich compositions there is a Mo<sub>ss</sub> + T<sub>2</sub> + Mo<sub>3</sub>Si three phase field as compared to a Nb<sub>ss</sub> + T<sub>2</sub> + T<sub>1</sub> three phase field. This demonstrates that the replacement of Mo by Nb destabilizes the Mo<sub>3</sub>Si phase in favor of the T<sub>1</sub> phase. At the same time the relatively narrow Mo<sub>ss</sub> + T<sub>2</sub> two phase field can be

compared to the relatively wide  $\text{Nb}_{ss} + \text{T}_2$  two phase field. As shown in Figure 5, the  $\text{BCC} + \text{T}_2 + \text{T}_1$  phase equilibrium is not available in the Mo-Si-B system. However, with solidification processing, a three phase  $\text{BCC} + \text{T}_2 + \text{T}_1$  eutectic structure (Figure 24) can be stabilized by the five-phase equilibrium:  $\text{Al}_5 + \text{L} \rightleftharpoons \text{BCC} + \text{T}_2 + \text{T}_1$

The stability of the  $\text{T}_2$  phase and the two-phase field of  $\text{BCC} + \text{T}_2$  can also be promoted in systems by means of an appropriate alloying strategy based on the combined geometry and electronic criteria. The development of a new three-phase mixture is unique due to the complementary nature of the properties of individual phase. The (Mo,Nb) BCC phase matrix provides the needed ductility, whereas the Nb-added  $\text{T}_2$  and  $\text{T}_1$  phases exhibit superior high temperature properties. The three-phase eutectic microstructure is advantageous due the fine microstructure scale, the ability to control the phase fractions, and the potential for directional solidification. Solidification processing allows for net-shape fabrication without the concern of residual porosity and inclusions that is common in powder synthesis. In addition, from the initial evaluation of the high temperature mechanical properties, it was confirmed that the three phase eutectic structure exhibited exceptionally high strength and creep resistance. For example, at  $1400^\circ\text{C}$  the flow stress at  $10^{-6}\text{s}^{-1}$  is over 600MPa [07PER]. However, the BCC solid solution phase in the eutectic did not provide sufficient low temperature ductility. As an approach to address this issue a modified microstructure design based upon a near eutectic microstructure with a BCC primary phase for increased ductility was identified as a goal and systematic alloy composition progression was developed. The alloy selection was based upon the key role of the overall metal content (i.e. Mo + Nb content) and the Nb/Mo ratio in selecting the solidification pathway to yield the goal microstructure of primary BCC dendrites and the  $\text{BCC} + \text{T}_2 + \text{T}_1$  eutectic.

Initial compositions (Figure 27a,b,c) with 75% metal (Mo,Nb) content yielded no primary BCC for increased ductility. However, as the Nb content is increased a more continuous BCC eutectic matrix is developed which is favorable due to the potential of increasing the volume fraction of the BCC phase in the eutectic cells. However, as the Nb addition is increased, less Mo is available to form the eutectic region resulting in the formation of a two-phase region ( $\text{BCC} + \text{T}_2$ ). The pro-eutectic two-phase region is a result of the relatively narrow  $\text{Mo}_{ss} + \text{T}_2$  two phase field in comparison to the relatively wide  $\text{Nb}_{ss} + \text{T}_2$  two phase field. At 75% metal content, the approximate upper Nb substitution limit is 60 at. % (Figure 27c). Increasing the metal content to 80% allows BCC dendrites to develop; however, at high Nb substitution (Figure 27d) the two-phase region still remains. Much of the Mo content is captured in the dendrites and too little Mo remains to form the three-phase eutectic.

Subsequent alloy compositions indicated the optimum metal level should be between 80% and 85% to facilitate the growth of primary BCC. In addition, the individual Mo and Nb content needs to be near balanced in order to stabilize the three-phase eutectic—too little Nb results in pure eutectic cells with no BCC primary, while too much Nb results in a depleted Mo content and two-phase regions. At 80% metal and 44 at. % Nb (Figure 27e) a near eutectic alloys with a BCC primary and some evidence of a  $\text{T}_2$  co-primary is produced. The overall volume fraction of the dendrites is slightly reduced from previous alloys, indicating a richer metal content within the eutectic. At 85% overall metal content (i.e. Mo+ Nb ), the microstructure (Figure 27f) achieves the near eutectic alloy with the primary BCC; however, small pockets of two-phase regions remain indicating the capture of Mo in the dendrites. An increase in Mo level at constant overall metal content (Figure 28) results in a eutectic alloy with BCC primary.

The resultant microstructure was annealed to determine the stability of the as-cast compositions. After a 1700°C, 25 hour anneal, the three phase eutectic cells have coarsened, but the volume fraction of primary BCC is maintained. The continuity of the BCC matrix that forms from the dendrites through the eutectic is critical for ductility and stress distribution. Furthermore, precipitates near the center of the dendrites are evident, indicating some of the captured Si, which substantially hardens the dendrites, is removed. Vickers hardness tests (1kgf) performed on the as-cast and annealed alloys indicate annealing softens the BCC phase as the hardness value drops from approximately 1200kg/mm<sup>2</sup> to 900kg/mm<sup>2</sup>. In addition, while the as-cast alloys display cracks propagating at the corners and blunting into the BCC dendrites, the annealed alloys display little to no crack propagation and an indication of BCC primary deformation around the indentation.

### **3. Summary of Research Highlights**

Refractory metal silicide phases are often considered to exhibit a relatively high stability as reflected in a high melting temperature. In fact, the high melting temperature and the potential for environmental stability from the development of an SiO<sub>2</sub> surface layer have attracted an increasing attention recently. A systematic examination of the refractory metal rich silicide phases as well as boride phases reveals some common structural features. The characteristic patterns have been shown to develop over certain well-defined ranges of atom sizes. Several of the arrangements yield a relatively dense packing that serves to maximize the metal-metal contacts within the structure. Within this group, the most efficient arrangement is developed in the T<sub>2</sub> phase. Along with the geometrical requirement that can be identified from the structural analysis, the observed alloying behavior in the silicide phases reveals that the electronic structure also plays a role and is, in some cases, an overriding factor in determining the relative phase stability. The influence of electronic structure factors can be represented in terms of the valence electron concentration per atom. Along with the specific geometric ranges that are associated with the different structures, there is also an electron concentration range that has been identified for given structures. In order to understand the observed alloying behavior within the silicides and borides it is necessary to include both the favorable geometric ranges and the allowed e/a ranges in the analysis. A similar set of geometrical and electronic criteria can be applied to the constitutional defect structures that develop from anti-site substitution. Moreover, the basis of the analysis has been tested in several case studies of solubility behavior and in the application of controlled alloying additions to alter the multicomponent phase stability. The selective TM alloying established from the current study has been applied to generate new series of light-weight TM-Mo-Si-B alloys (TM= Ti or Cr) in the bulk form. The alloys possess not only the advantage of low weight density (below that of Ni-super alloys, i.e < 9 g/cm<sup>3</sup>), but also offer both oxidation and thermal protections *in-situ* by the formation of distinct layers of both ultra-high temperature metal oxides (e.g TiO<sub>2</sub>, ZrO<sub>2</sub>)- for thermal protection- and boron-doped silica as an oxidation barrier. To provide key kinetics data diffusion couples consisting of binary boride and silicide phases have been used to determine the diffusion kinetics of T<sub>2</sub> phase development. The measurements indicate a 10<sup>3</sup> smaller integrated interdiffusion coefficient for Si in T<sub>2</sub> compared to Mo<sub>5</sub>Si<sub>3</sub> due mainly to the larger activation energy for Si diffusion. This finding is consistent with the remarkable stability of microstructures based upon the T<sub>2</sub> phase.



Based upon our foundation of phase stability including measurement of the phase equilibria from 1600 to 1950°C, we have identified quaternary Mo-Nb-Si-B alloys with a monovariant eutectic reaction to yield a three phase  $(\text{Mo}(\text{Nb})+\text{T}_2+\text{T}_1)$  fine scale eutectic microstructure. Preliminary mechanical property testing (in collaboration with Professor S. Kumar of Brown University) has demonstrated that these alloys have exceptional high temperature strength and creep resistance comparable to that of ultra-high temperature ceramics. Moreover, the alloy design can be modified to provide for a continuous BCC matrix phase with low temperature ductility. In effect the stability analysis provides essential guidance to develop new multiphase microstructures with superior oxidation resistance and mechanical properties. These advances also offer new options to overcome the materials processing challenges.

A high density of vacancies develops in the  $\text{T}_2$  phase of a Mo-10Si-20B alloy during solidification. Upon high temperature annealing, these vacancies combine to form a network of edge dislocations with Burgers vectors of  $\langle 100 \rangle$  and  $\langle 110 \rangle$ , which then provide heterogeneous sites for subsequent Mo precipitation. In collaboration with Profesor A. Freeman we have analyzed the observed dislocation character in terms of the bonding energetics to provide important new insight on the dislocation and deformation behavior in the  $\text{T}_2$  phase. At the same time the first principles calculations indicate that several slip systems have relatively close energies that suggests with suitable alloying it may be possible to promote operation of multiple systems that can benefit low temperature ductility.

Overall, there has been significant progress in the current work in advancing the understanding of Mo-Si-B alloys, but there are some critical issues concerning the materials processing, low temperature ductility and behavior of non-stoichiometric phases that must be addressed to realize the potential performance enhancements. In addressing these critical issues, the stability analysis provides essential guidance to develop new multiphase combinations and new microstructures with superior oxidation resistance and mechanical properties.

#### **4. Personnel Supported**

|                   |                        |
|-------------------|------------------------|
| John H. Perepezko | Principal Investigator |
| Ridwan Sakidja    | Research Associate     |
| Seth Imhoff       | Graduate Student       |
| Megan Jarosinski  | Graduate Student       |

#### **5. Publication List**

1. R. Sakidja and J. H. Perepezko, "Alloying and microstructure stability in the high-temperature Mo-Si-B system", *Journal of Nuclear Materials*, v. 366, Issue 3, p. 407-416 (2007).
2. J. H. Perepezko, R. Sakidja and K. S. Kumar, "Mo-Si-B Alloys for Ultrahigh Temperature Applications", Chapter 13 in *Advanced Structural Materials: Properties, Design Optimization, and Applications*, edited by W. Soboyejo (CRC Press, Boca Raton, FL, 2007) pp. 437-473.
3. N. Sekido, R. Sakidja and J. H. Perepezko, "Precipitation behavior of (Mo) phase on dislocations in  $\text{Mo}_5\text{SiB}_2$  phase", *Proceedings of an International Conference on Solid-Solid Phase Transformations in Inorganic Materials 2005*, , pt. 1, p. 357-362, vol.1 (2006).
4. S. Kim and J.H. Perepezko, "Interdiffusion Kinetics in the  $\text{Mo}_5\text{SiB}_2$  ( $\text{T}_2$ ) Phase", *Journal of Phase Equilibria and Diffusion*, v. 27, No.6, p. 605-613 (2006).
5. N. Sekido, R. Sakidja and J. H. Perepezko, "Annealing Response of Point Defects in Off-Stoichiometric  $\text{Mo}_5\text{SiB}_2$  Phase", *Intermetallics*, 15, 1268 (2007).
6. J. H. Perepezko, R. Sakidja, S. Kim and N. Sekido, "Phase Stability and Structural Defects in High-Temperature Mo-Si-B Alloys", *Acta Materialia*, 56, 5223, (2008)

7. "Deformation behavior of  $\text{Mo}_5\text{SiB}_2$ " N.I. Medvedeva, O.Yu. Kontsevoi, J.H. Perepezko and A.J. Freeman, Phys. Rev. Lett., submitted.

## 6. Transitions

1. Meetings, Conferences, Seminars
  - a. Knolls Atomic Power Laboratory, Schenectady, NY, September 2006, "Phase Stability and Microstructure Development in High Temperature Mo-Si-B Alloys".
  - b. TMS Fall Meeting, Cincinnati, OH, September 2006. "Microstructure Design and High Temperature Applications of Mo-Si-B Alloys".
  - c. AFOSR Contractors annual meeting, Arlington, VA, November 2006.-Presentation: "The Analysis and Modeling of Phase Stability and Multiphase Designs in High Temperature Refractory Metal-Silicon-Boron Alloys"
  - d. TMS Annual Meeting, Orlando, FL February 2007, "High Temperature Mo-Si-B Alloys and Coatings".
  - e. Symposium on Phase Stability and Defect Structures in Advanced Materials, Orlando, FL., March 2007, "Phase Stability and Structural Defects in High Temperature Mo-Si-B Alloys".
  - f. Tokyo Institute of Technology, May 2007, "High Temperature Mo-Si-B Alloys: Phase Stability and Oxidation Performance".
  - g. Y.A. Chang Symposium, Orlando, FL, 2007, "Phase Stability and Structural Defects in High-Temperature Mo-Si-B.
  - h. TMS Annual 2008 Meeting, New Orleans, LA, 2008, "High Temperature Mo-Si-B Alloy Design and Microstructure".
2. Consultative and Advisory – None
3. Technology Assists, Transitions and Transfers
  - a. Throughout the program we maintain a close contact with D. Berczik of Pratt & Whitney who is leading a major Air Force/Navy sponsored project on high temperature Mo-Si-B alloys.
  - b. As part of an STTR program we are working with Pittsburgh Materials Technology Inc. to transition Mo-Si-B alloys into commercial use.

## 7. Patents

None

## 8. Honors/Awards

John H. Perepezko : ASM-International Fellow, TMS Fellow, National Academy of Engineering.  
Megan Jarosinski: NDSEG Fellowship Award (9/08).

## 9. References

- |         |   |
|---------|---|
| [31HAG] | Hagg, G. <i>Zeitschrift für physikalische Chemie. Abteilung B</i> 1931, 12, 33.                     |
| [57NOW] | Nowotny, H.; Dimakopoulou, E.; Kudielka, H. <i>Monatshefte fuer Chemie</i> 1957, 88, 180.           |
| [57NOW] | Nowotny, H.; Kieffer, R.; Benesovsky, F. <i>Planseeberichte fuer Pulvermetallurgie</i> 1957, 5, 86. |
| [58ARO] | Aronsson, B. <i>Acta Chemica Scandinavica</i> 1958, 12, 31.   |
| [59ARO] | Aronsson, B.; Lundgren, G. <i>Acta Chem. Scandinavica</i> 1959, 13, 433 - 443.                      |

- [60NOW] Nowotny, H.; Benesovsky, F.; Rudy, E.; Wittmann, A. *Monatshefte Fuer Chemie* 1960, 91, 975-990.
- [60PAU] Pauling, L. *The Nature of the Chemical Bond*; 3 ed.; Cornell University Press: Ithaca, NY, 1960.
- [74VIT] Vitek, V. *Cryst. Latt. Def.* 5, 1 (1974).
- [77PET] Pettifor, D. G. *Journal of Physics F* 1977, 7, 613.
- [79KAU] Kaufman, L. CALPHAD: Computer Coupling of Phase Diagrams and Thermochemistry, 1979, 3(1): 45 - 76.
- [80ISH] Ishida, Y.; Ishida, H.; Kohra, K.; Ichinose, H. *Philosophical Magazine* 1980, 42A, 453.
- [83OHN] Ohnishi, S.; Freeman, A. J.; Weinert, M. *Phys. Rev. B* 1983, 28, 6741.
- [83WIL] Williams, A. R.; Gelatt, C. D.; Connolly, J. W. D.; Moruzzi, V. L. *Alloy Phase Diagram*; North-Holland: New York, 1983; pp 17.
- [84FRA] Franceschi, E. A.; Ricaldone, F. *Revuc de Chimic Minerale* 1984, 21, 202.
- [84SKR] Skriver, H. L. *The LMTO Method*; Springer: Berlin, 1984.
- [85FU] Fu, C. L.; Freeman, A. J.; T. Oguchi *Phys. Rev. Lett.* 1985, 54, 2700.
- [87XU] Xu, J.-H.; Oguchi, T.; Freeman, A. J. *Phys. Rev. B* 1987, 35.
- [89BOE] Boer, F. R.; Boom, R.; Mattens, W. C. M.; Miedema, A. R.; Niessen, A. K. *Cohesion in Metals - Transition Metal Alloys*; Elsevier Science, 1989.
- [89HAR] Harrison, W. A., *Electronic Structure and the Properties of Solids*; Dover: New York, 1989.
- [89XU] Xu, J.; Freeman, A. J. *Physical Review B* 1989, 40, 11927.
- [90XU] Xu, f.-H.; Freeman, A. J. *Phys. Rev. B* 1990, 41, 12 553.
- [94MCM] McMahan, A. K.; Klepeis, J. E.; Schilfgaarde, M. v.; Methfessel, M. *Physical Review B* 1994, 50, 10742.
- [96DAY] Dayananda, M. A. Average Effective Interdiffusion Coefficients and the Matano Plane Composition., *Metall. Mater. Trans. A* 1996, 27A, 2504-2509.
- [97BER] Berzcik, D. M. Oxidation Resistant Molybdenum Alloys; U.S. Patent No. 5, 693, 156, 1997.
- [97NUN] Nunes, C.A., R. Sakidja, and J.H. Perepezko, in *Structural Intermetallics 1997*, M.V. Nathal, et al., Editors. 1997, TMS: Warrendale, PA. p. 831.
- [97NUN] Nunes, C. A.; Sakidja, R.; Perepezko, J. H. *Structural Intermetallics 1997*; TMS: Warrendale, PA, 1997; pp 831.
- [97PER] Perepezko, J. H.; Nunes, C. A.; Yi, S. H.; Thoma, D. J. *High Temperature Ordered Intermetallic Alloys VII*; MRS: Pittsburgh, PA, 1997; pp 1.
- [97PET] Petrovic, J. J. High Temperature Structural Silicides. *21st Annual Conference on Composites, Advanced Ceramics, Materials and Structures - A*, 1997; pp 3-17.
- [97ZHU] Zhu, J. H.; Liaw, P. K.; Liu, C. T. Effect of electron concentration on the phase stability of NbCr<sub>2</sub>-based Laves phase alloys. *Mater. Sci. and Eng.* 1997, A239-240, 260-264.



- [99DAY] Dayananda M. A. and Y. H. Sohn, A New Analysis for the Determination of Ternary Interdiffusion Coefficients from a Single Diffusion Couple, *Metall. Mater. Trans. A*, 1999, 30A, p 535-543
- [99DAY] Dayananda, M. A.; Sohn, Y. H. *Metall. Mater. Trans. A* 1999, 30A, 535.
- [99FAN] Fan X, Hack K, Ishigaki T. *Mater Sci Eng* 2000;278A:46-53.
- [99FU] Fu, C. L., X. Wang, et al., *Intermetallics*, 1999, 7: 179 -184.
- [99SAK] Sakidja, R., et al., in *High Temperature Ordered Intermetallic Alloys VIII*, E.P. George, M. Yamaguchi, and M.J. Mills, Editors. 1999, MRS: Pittsburgh, PA. p. KK6.3.1.
- [99SAK] Sakidja, R.; Sieber, H.; Perepezko, J. H. *Phil. Mag. Lett.* 1999, 79, 351.
- [99SCH] Schneibel, J.H., et al., *Mater. Sci. and Eng. A*, 1999. 1-2: p. 78.
- [99TOR] Tortorici, P. C.; Dayananda, M. A. Growth of Silicides and Interdiffusion in the Mo-Si System. *Metall. Mater. Trans. A* 1999, 30A, 545-550.
- [00FOU] Fournelle J. H., J. J. Donovan, S. Kim and J. H. Perepezko, Analysis of Boron by EPMA: Correction for Dual Mo and Si Interferences for Phases in the Mo-Si-B System, *Inst. Phys. Conf. Ser.*, 2000, No 165, p 425-426
- [00FU] Fu, C. L.; Wang, X. *Phil. Mag. Letters* 2000, 80, 683.
- [00HUE] Huebsch, J. J.; Kramer, M. J.; Zhao, H. L.; Akinc, H. *Intermetallics* 2000, 8, 143.
- [00NUN] Nunes, C. A.; Sakidja, R.; Dong, Z.; Perepezko, J. H. *Intermetallics* 2000, 8, 327.
- [00ROS] Rosales, I.; Schneibel, J. H. *Intermetallics* 2000, 8, 885.
- [00SAK] Sakidja, R.; Myers, J.; Kim, S.; Perepezko, J. H. *Int. J. Refrac. Met. Hard Mater.* 2000, 18, 193.
- [00ZHA] Zhao, J.-C.; Bewlay, B. P.; Jackson, M. R.; Chen, Q. *Journal of Phase Equilibria* 2000, 21, 40-45.
- [01FIE] Field, F. D.; Thoma, D. J.; Cooley, J. C.; Chu, F.; Fu, C.-L. et al. *Intermetallics* 2001, 9, 863.
- [01KIM] Kim, S.; Sakidja, R.; Dong, Z.; Perepezko, J. H.; Kim, Y. W. *High Temperature Ordered Intermetallic Alloys IX*; MRS: Pittsburg, PA, 2001; pp N5.42.41.
- [01KIM] Kim S., R. Sakidja, Z. Dong, J. H. Perepezko and Y. W. Kim, Growth of the Mo<sub>5</sub>SiB<sub>2</sub> Phase in a Mo<sub>5</sub>Si<sub>3</sub>/Mo<sub>2</sub>B Diffusion Couple, *Mater. Res. Soc. Symp. Proc.*, 2001, 646, p N5.42.1-N5.42.6
- [01PER] Perepezko, J. H.; Sakidja, R.; Kim, S.; Dong, Z.; Park, J. S. *International Symposium on Structural Intermetallics*; The Materials Society, Warrendale, PA: Jackson Hole, WY, 2001; pp 505.
- [01PER] Perepezko, J. H.; Sakidja, R.; Kim, S. *High Temperature Ordered Intermetallic Alloys IX*; MRS: Pittsburgh, PA, 2001; pp N4.5.1.
- [01RAW] Rawn, C. J.; Schneibel, J. H.; Hoffmann, C. M.; Hubbard, C. R. *Intermetallics* 2001, 9, 209 - 216.
- [02FER] Fernandes, P. B.; Coelho, G. C.; Ferreira, F.; Nunes, C. A.; Sundman, B. Thermodynamic modeling of the Nb-Si system. *Intermetallics* 2002, 10, 993-999.
- [02KAT] Katrych, S.; Grytsiv, A.; Bondar, A.; Rogl, P.; Velikanova, T. et al. *J. of Alloys and Compounds* 2002, 347, 94-100.
- [02SCH] Schneibel, J. H.; Kramer, M. J.; Easton, D. S. *Scripta Mater.* 2002, 46, 217.

- [02WOO] Woodward, C. and S.I. Rao, Phys. Rev. Lett. **88**, 216402 (2002).
- [03DIM] Dimiduk, D. M.; Perepezko, J. H. *MRS Bulletin*, **28**, 639 (2003).
- [03FU] Fu, C. L.; Schneibel, J. H. *Acta Materialia* 2003, **51**, 5083.
- [03SAK] Sakidja, R. *Phase stability and transition metal addition in Mo-Si-B alloys*. In *Dept. of Materials Science & Engineering*; University of Wisconsin-Madison: Madison, 2003; pp 159.
- [04COC] Cochran, P. c. w. P. J. 2004.
- [04ITO] Ito K., T. Hayashi, M. Yokobayashi and H. Numakura, Evolution Kinetics and Microstructure of  $\text{MoSi}_2$  and  $\text{Mo}_5\text{Si}_3$  Surface Layers on Two-phase Mo-9Si-18B Alloy During Pack-cementation and High-temperature Oxidation, *Intermetallics*, 2004, **12**, p 407-415
- [04JEH] Je'hanno, P.; Heilmaier, M.; Kestler, H. *Intermetallics* 2004, **12**, 1005.
- [04RAM] Ramos, A. S.; Nunes, C. A.; Rodrigues, G.; Suzuki, P. A.; Coelho, G. C. et al. *Intermetallics* 2004, **12**, 487-491.
- [05HAY] Hayashi, T.; Ito, K.; Numakura, H. Reaction Diffusion of  $\text{MoSi}_2$  and  $\text{Mo}_5\text{Si}_3$ . *Intermetallics* 2005, **13**, 93-100.
- [05RAW] Rawn, C. J.; Schneibel, J. H.; Fu, C. L. *Acta Materialia* 2005, **53**, 2431-2437.
- [05TRI] Trinkle, D. and C. Woodward, *Science* **310**, 1665 (2005).
- [05YAN] Yang, Y.; Chang, Y. A.; Tan, L.; Cao, W. *Acta Materialia* 2005, **53**, 1711-1720.
- [05YAN] Yang, Y.; Chang, Y. A. *Intermetallics* 2005, **13**, 121-128.
- [06DHE] Dheeradhada, V. S.; Johnson, D. R.; Dayananda, M. A. *J. Phase Equilibria and Diffusion* 2006, **27**, 582.
- [06JEH] Jehanno, P.; Heilmaier, M.; Saage, H.; Heyse, H.; Boning, M. et al. *Scripta Mater.* 2006, **55**, 525-528.
- [06JEH] Je'hanno, P.; Heilmaier, M.; Saage, H.; Heyse, H.; Boning, M. et al. *Scripta Materialia*
- [06KIM] Kim, S.; Perepezko, J. H. *J. Phase Equilibria and Diffusion* 2006, **27**, 605.
- [07PER] Perepezko, J. H.; Sakidja, R.; Kumar, K. S. Mo-Si-B Alloys for Ultrahigh Temperature Applications. *Advanced Structural Materials: Properties, Design Optimization, and Applications*; CRC Press: Boca Raton, FL, 2007; pp 437-473.

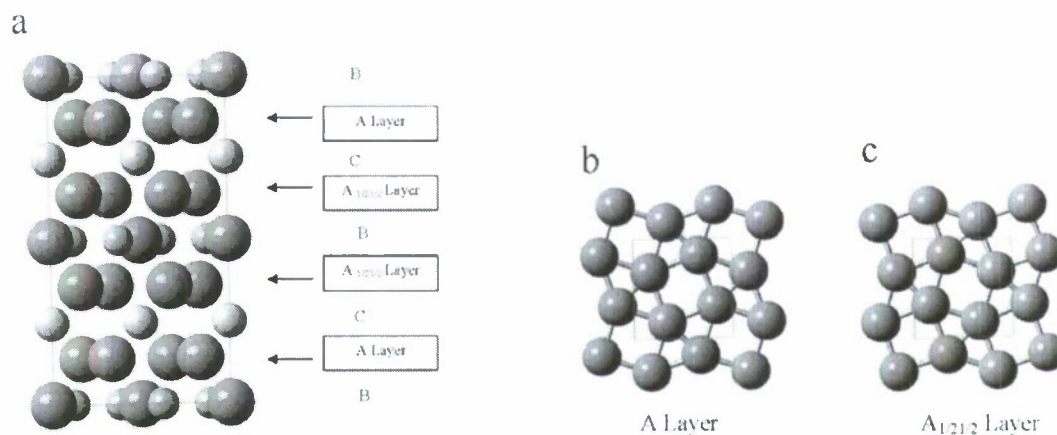


Figure 1:  $T_2$  Crystal Structure for  $Mo_5SiB_2$  (illustrated in a) comprised of the stacking of a Mo only atomic layer (A or  $A_{1/2 1/2}$  layer), a Mo + B atomic layer (B) and a Si only atomic layer (C). The atomic arrangement of the A layer and  $A_{1/2 1/2}$  layer are illustrated in b and c.

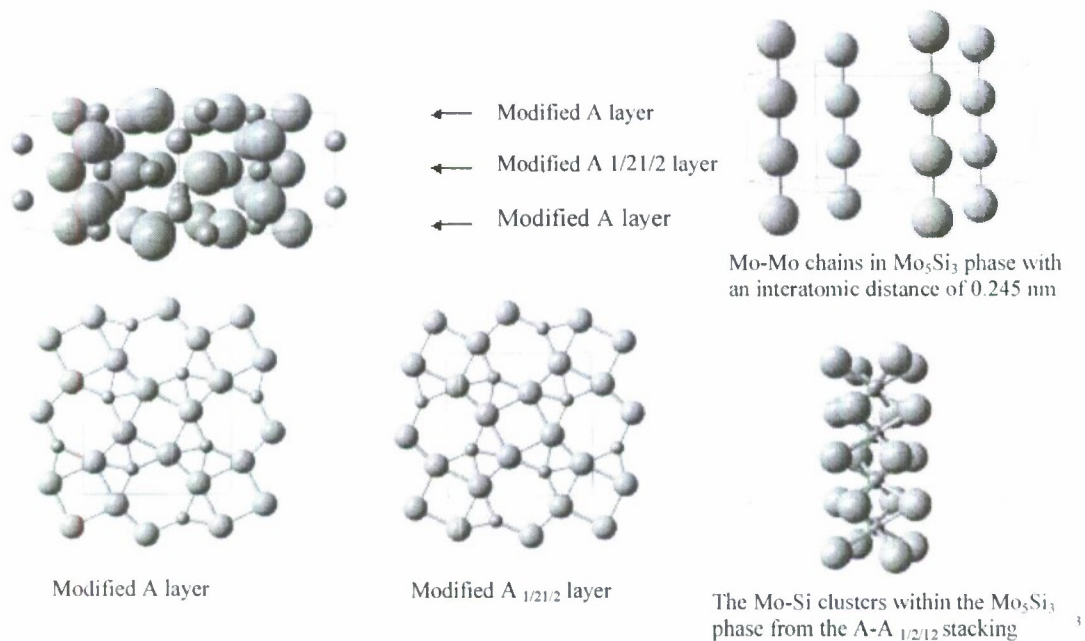


Figure 2: Structure of  $Mo_5Si_3$  ( $T_1$ ) phase showing the alternating sequence of modified A and  $A_{1/2 1/2}$  layers. The atomic arrangements of the modified A layer and  $A_{1/2 1/2}$  layer are illustrated.



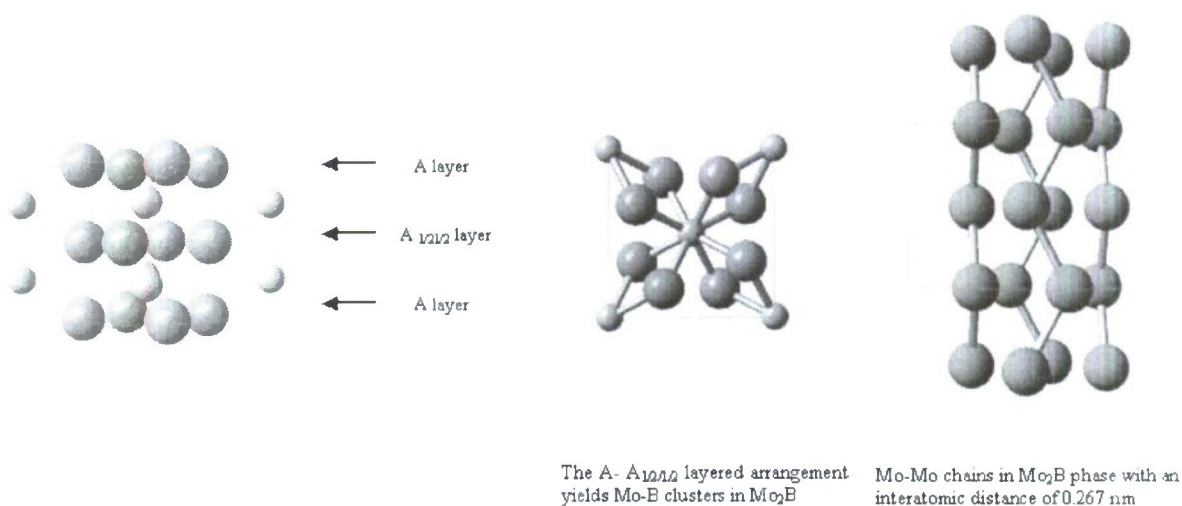


Figure 3: Crystal Structure of  $Mo_2B$  phase showing the alternating sequence of the modified A and  $A_{1/2}A_{1/2}$  layers bordering the B only layers. The crystal structure is also characterized by the presence of Mo-Mo vertical chains similar to those present in the  $T_1$  phase (see Figure 2).

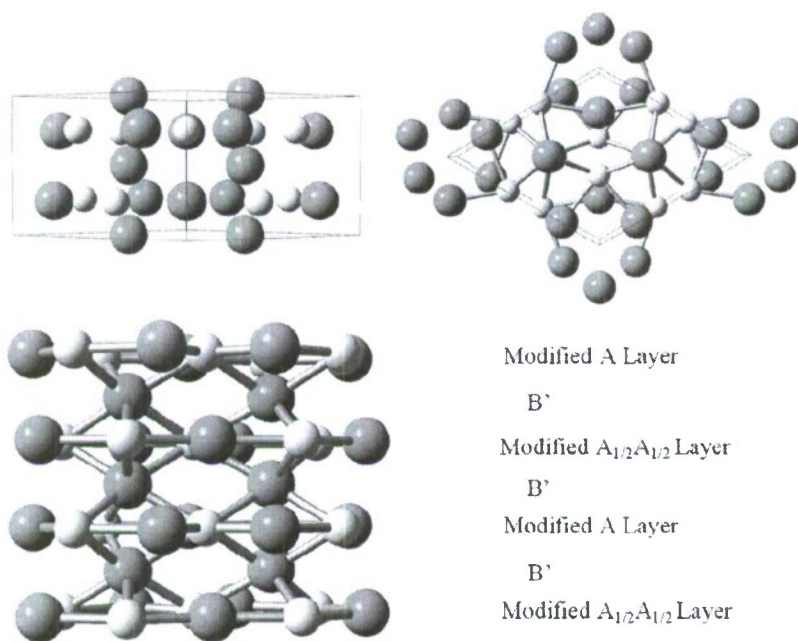


Figure 4: Crystal Structure of  $Ti_5Si_3$  ( $D8_8$ ) phase showing the alternating sequence of the modified A and  $A_{1/2}A_{1/2}$  layers bordering the 2/3- filled Mo-only B' layer.

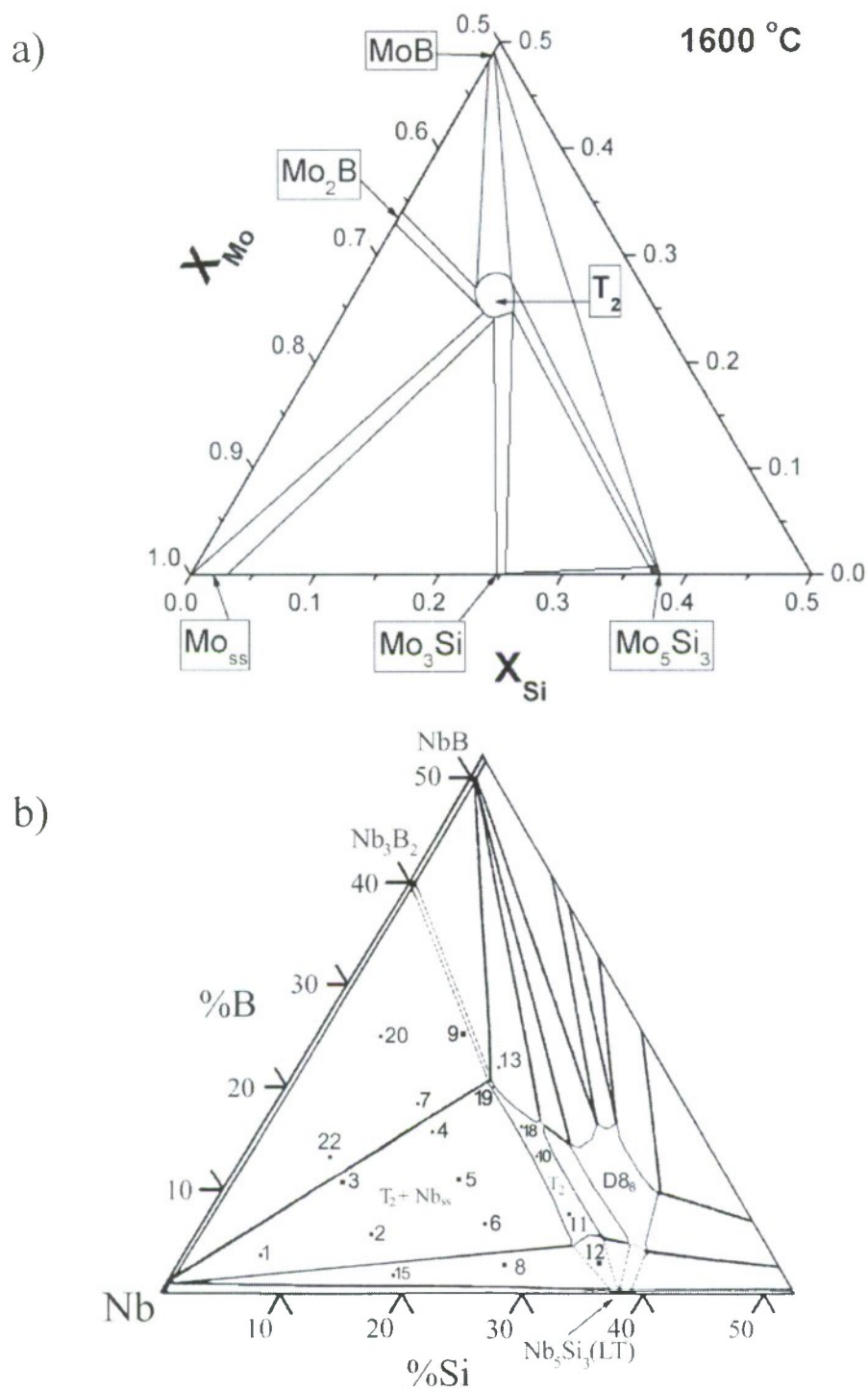


Figure 5: a) Mo-Si-B and b) Nb-Si-B isothermal sections for Mo,Nb-rich compositions at 1600°C.

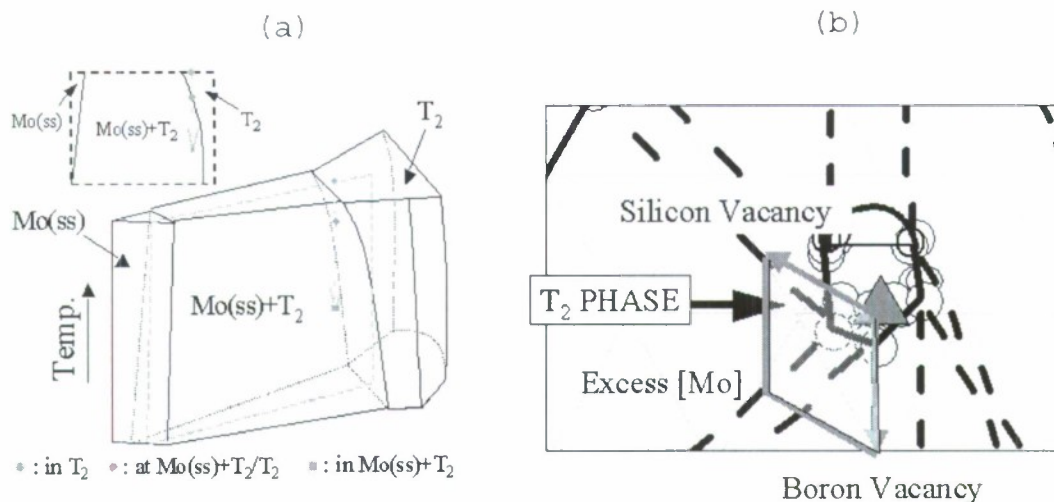


Figure 6: a) Schematic of Mo(ss)- $T_2$  section with compositions variation with temperature that allows for the Mo(ss) precipitation reaction in the  $T_2$  phase and b) constitutional defect structures in  $Mo_5SiB_2$  ( $T_2$ ) phase involving the formation of both Si and B vacancies. The net effect results in a compositional shift toward Mo-rich region or Mo excess (i.e.  $Mo_5Si_{1-x}B_{2-y}$  with  $x$  and  $y$  as the vacancy concentration of Si and B respectively). Subsequent annealing treatment at high temperatures yields a Mo(ss) precipitation. Triangle denotes the stoichiometric  $T_2$  composition.

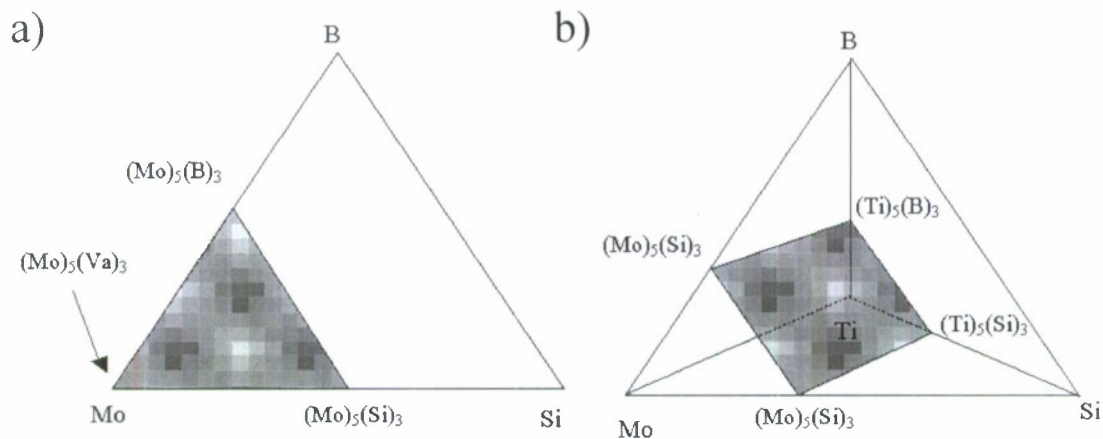


Figure 7: Areas covered by the end members of thermodynamic two-sublattice models for the  $T_2$  phase in a) ternary Mo-Si-B – a triangle area of  $(Mo)_5(Va)_3$ - $(Mo)_5(Si)_3$ - $(Mo)_5(B)_3$  and b) Mo-Ti-Si-B system – a rectangular slice of  $(Mo)_5(Si)_3$ - $(Mo)_5(B)_3$ - $(Ti)_5(Si)_3$ - $(Ti)_5(B)_3$ .



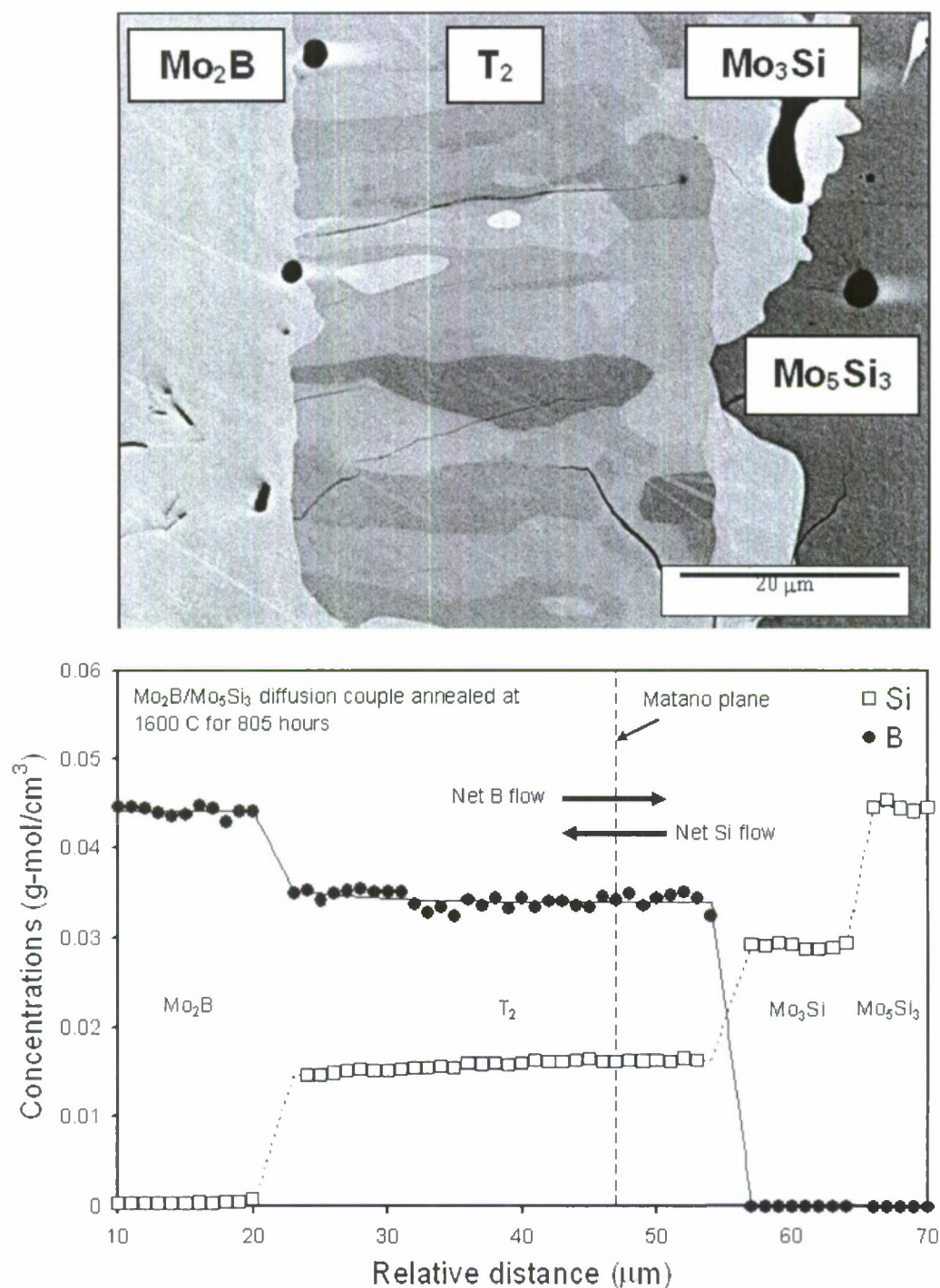


Figure 8: a) BSE images of cross-sections of the  $\text{Mo}_2\text{B}/\text{Mo}_5\text{Si}_3$  diffusion couples heat-treated at  $1600^\circ\text{C}$  for 805 hrs, b) Concentration profiles of Si and B obtained from EPMA measurements on the  $\text{Mo}_2\text{B}/\text{Mo}_5\text{Si}_3$  diffusion couple annealed at  $1600^\circ\text{C}$  for 805 hours. Solid and dotted smooth lines are drawn by numerically fitting a polynomial equation on concentration profile data.

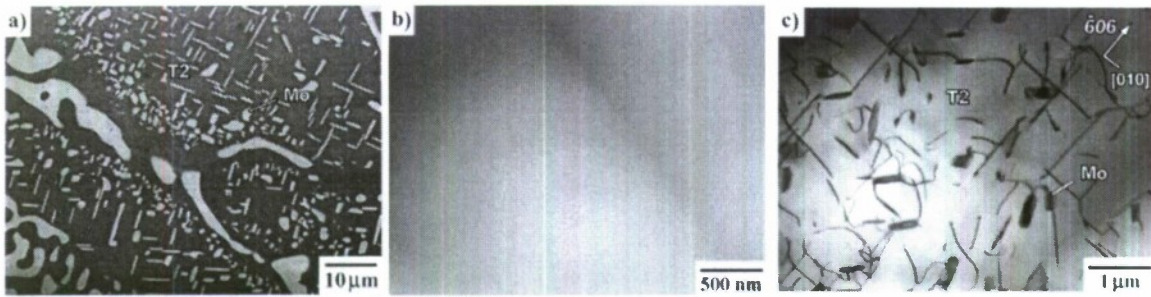


Figure 9: a). SEM Micrograph of a Mo-10Si-20B alloy annealed at 1600 °C for 150 hrs, (b) TEM micrographs of an as-cast Mo-10Si-20B alloy and (c) a Mo-10Si-20B alloy annealed at 1550°C for 20 hours.

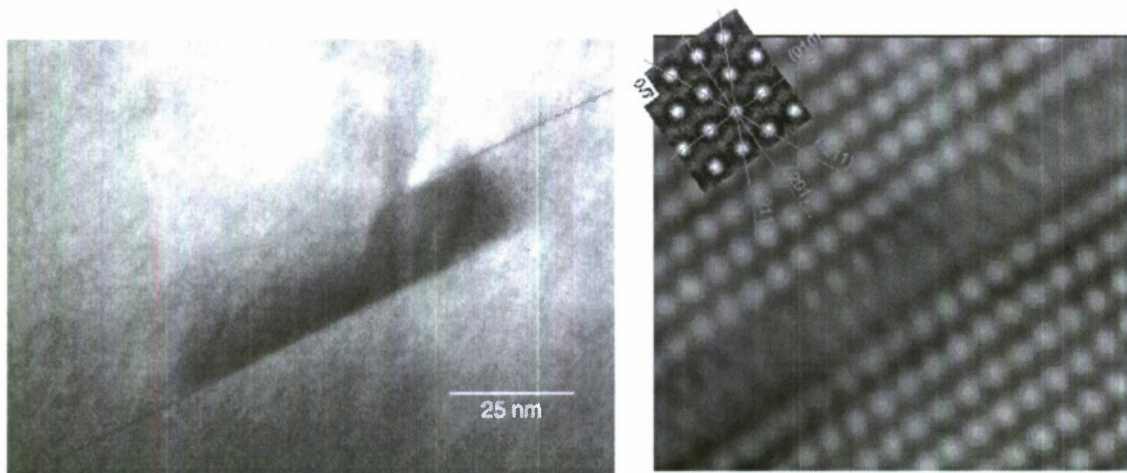


Figure 10: Stacking faults are present in a) Bright field TEM image of the  $T_2$  phase b) HRTEM analysis showing a the presence of a stacking fault along the (010) planes

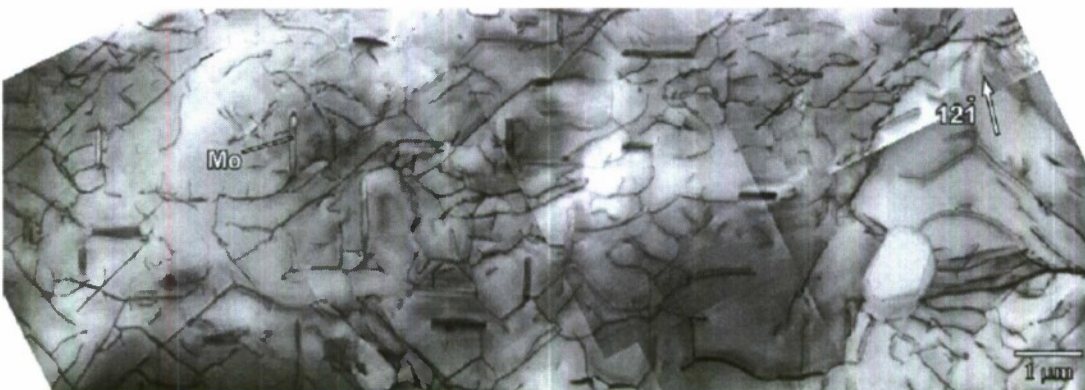


Figure 11: Bright field TEM image in annealed Mo-10Si-20B annealed at 1550°C for 20 hours showing the dislocation networks.



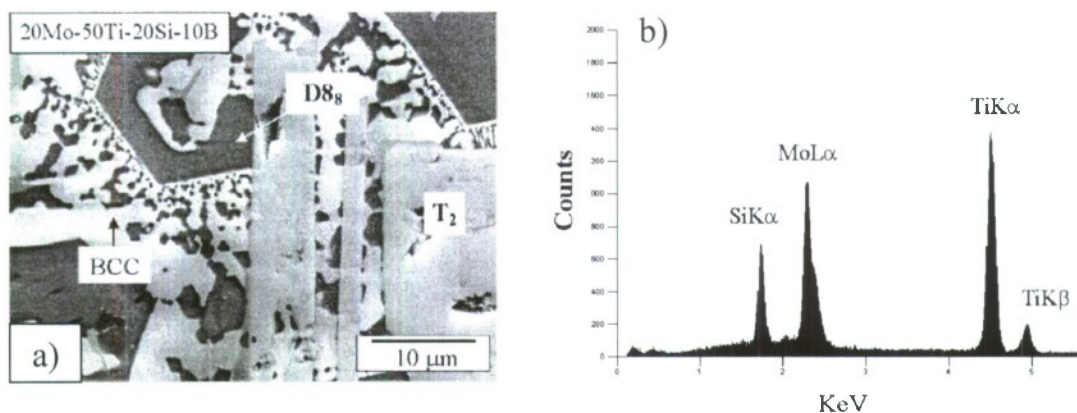


Figure 12: a) Back Scattered SEM image of Ti-substituted Mo-Si-B alloy with a nominal composition of Mo-50Ti-20Si-10B 9at. %) and b) EDS spectrum on the *Ti-rich* T<sub>2</sub> Phase.

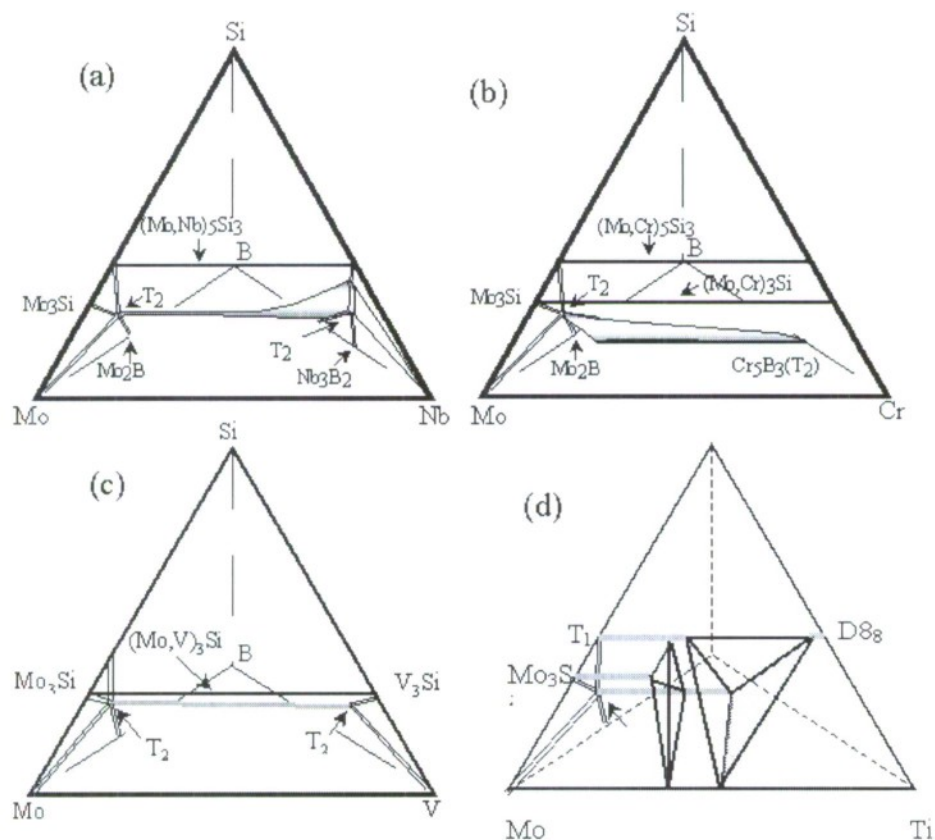


Figure 13: Schematic illustrations of observed solubility for selected transition metal in both the BCC and the T<sub>2</sub> phase in the Quaternary Mo-TM-Si-B Systems of a) Mo-Nb-Si-B b) Mo-Cr-Si-B, c) Mo-V-Si-B d) Mo-Ti-Si-B where the Ti substitution for Mo in the T<sub>2</sub> phase is extensive enough to form a Ti-rich T<sub>2</sub> phase and to stabilize a three-phase region of BCC + T<sub>2</sub> + D8<sub>8</sub> (shaded area)



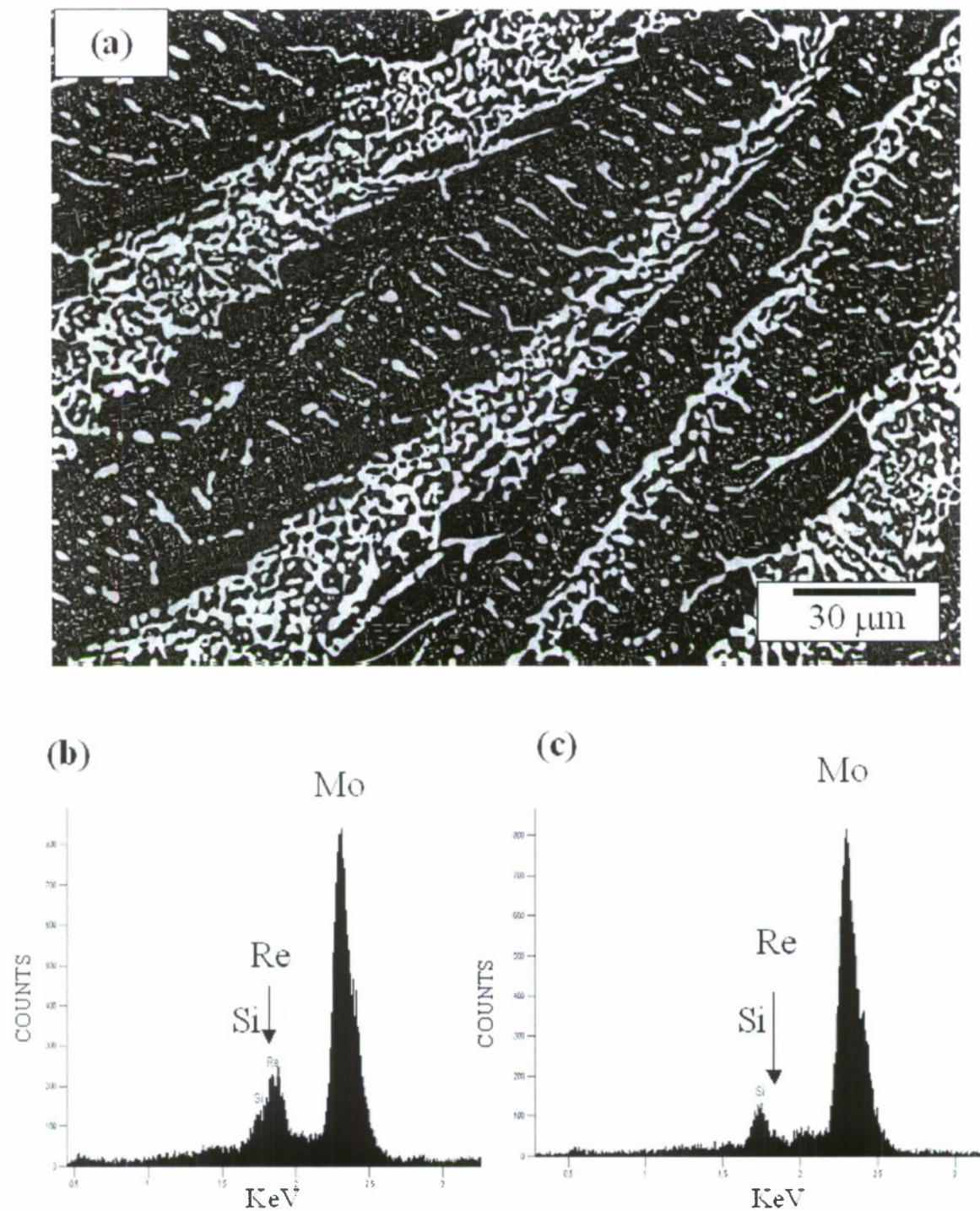


Figure 14: a) BSE image of Mo-5Re-10Si-20B alloy microstructure after annealing at 1600°C (150 h) showing the T<sub>2</sub> (dark) and BCC (bright) phases. The EDS spectrum in (b) indicates 8 at. % solubility of Re in the BCC phase. In contrast, the spectrum from the T<sub>2</sub> phase (c) indicates the low solubility of Re (less than 1 at. %).

|    |  | I A                        | II A  | III B   | IV B   | V B                                  | VIB                                   | VII B   | VIII                              | IB                       | II B                     | III A  | IV A   | V A                        | VI A                     |
|----|--|----------------------------|---|---|--|--------------------------------------|---------------------------------------|---|-----------------------------------|--------------------------|--------------------------|--|--|----------------------------|--------------------------|
| Li | Be   |                            |   |   |  |                                      |                                       |   |                                   |                          |                          |  |  |                            |                          |
| Na | Mg   |                            |   |   |  |                                      |                                       |   |                                   |                          |                          |  |  |                            |                          |
|    |  |                            |   |   |  |                                      |                                       |   |                                   |                          |                          |  |  |                            |                          |
|    |  |                            |   |   |  |                                      |                                       |   |                                   |                          |                          |  |  |                            |                          |
| K  | Ca   | Sc                         | Ti  | V   | Cr   | Mn                                   | Fe                                    | Co  | Ni                                | Cu                       | Zn                       | Ga   | Ge   | As                         | Se                       |
|    | $\text{Ca}_3\text{Si}_2$<br>$\text{Ca}_2\text{Ge}_3$<br>$\text{Ca}_3\text{Sn}_2$ |                            | $(\text{Ti}, \text{TM})_2(\text{Si}, \text{B})_3$ | $\text{V}_3\text{SiB}_2$<br>$(\text{V}, \text{TM})_2(\text{Si}, \text{B})_3$<br>$\text{V}_4\text{WSiB}_2$             | $\text{Cr}_3\text{B}_3$<br>$\text{Cr}_2\text{PB}_2$<br>$(\text{Cr}, \text{TM})_2(\text{Si}, \text{B})_3$                       | $\text{Mn}_3\text{SiB}_2$            | $\text{Fe}_3\text{SiB}_2$             | $\text{Co}_3\text{SiB}_2$<br>$\text{Co}_2\text{PB}_2$ | $\text{RE}_3\text{SnNi}_2$        |                          | $\text{Ca}_2\text{Zn}_3$ | $\text{Ca}_2\text{Ge}_3$                             | $\text{TM}_2\text{Ge}_3$<br>$\text{Ca}_2\text{Ge}_3$<br>$\text{RE}_2\text{Ge}_3$<br>$\text{TM}_2\text{Ge}_2\text{B}$ |                            |                          |
| Rb | Sr   | Y                          | Zr  | Nb  | Mo   | Tc                                   | Ru                                    | Rh  | Pd                                | Ag                       | Cd                       | In   | Sn   | Sb                         | Te                       |
|    | $\text{Sr}_2\text{Si}_3$<br>$\text{Sr}_2\text{Ge}_3$<br>$\text{Sr}_2\text{Sn}_3$ | $\text{Y}_3\text{SnNi}_2$  | $(\text{Zr}, \text{TM})_2(\text{Si}, \text{B})_3$ | $\text{Nb}_3\text{Si}_3$<br>$\text{Nb}_2(\text{Si}, \text{B})_3$<br>$(\text{Nb}, \text{TM})_2(\text{Si}, \text{B})_3$ | $\text{Mo}_3\text{SiB}_2$<br>$(\text{Mo}, \text{TM})_2(\text{Si}, \text{B})_3$   |                                      | $\text{RE}_2(\text{Ru}, \text{Si})_3$ | $\text{RE}_2(\text{Rh}, \text{Si})_3$                 |                                   | $\text{Ca}_2\text{Ag}_3$ | $\text{Sr}_2\text{Cd}_3$ | $\text{In}_3\text{Sb}_3$<br>$\text{Sr}_2\text{In}_3$ | $\text{RE}_3\text{SnNi}_2$<br>$\text{Sr}_2\text{Sn}_3$   | $\text{RE}_3\text{SbNi}_2$ | $\text{Ti}_2\text{Te}_3$ |
| Cs | Ba   | Lu                         | Hf  | Ta  | W  | Re                                   | Os                                    | Ir  | Pt                                | Au                       | Hg                       | Tl   | Pb   | Bi                         | Po                       |
|    | $\text{Ba}_2\text{Ge}_3$<br>$\text{Ba}_2\text{Sn}_3$                             | $\text{Lu}_3\text{SnNi}_2$ | $(\text{Hf}, \text{TM})_2(\text{Si}, \text{B})_3$ | $\text{Ta}_2\text{Si}_3$<br>$\text{Ta}_2\text{Ge}_2\text{B}$<br>$(\text{Ta}, \text{TM})_2(\text{Si}, \text{B})_3$     | $\text{W}_2(\text{Si}, \text{B})_3$<br>$(\text{W}, \text{TM})_2\text{B}_3$<br>$(\text{W}, \text{TM})_2(\text{Si}, \text{B})_3$ | $(\text{Re}, \text{Cr})_2\text{B}_3$ |                                       | $\text{RE}_2(\text{Rh}, \text{Ce})_3$                 | $\text{RE}_2\text{Pt}_3\text{Bi}$ | $\text{Ba}_2\text{Au}_3$ | $\text{Ca}_2\text{Hg}_3$ | $\text{Ti}_2\text{Te}_3$<br>$\text{Sr}_2\text{Tl}_3$ | $\text{Sr}_2\text{Pb}_3$<br>$\text{Ba}_2\text{Pb}_3$<br>$\text{RE}_3\text{PbNi}_2$                                   |                            |                          |

## Lanthanide Series:

|  |  |  |  |    |  |  |  |  |  |                            |                            |    |    |
|--|--|--|--|----|--|--|--|--|--|----------------------------|----------------------------|----|----|
| La   | Ce   | Pr   | Nd   | Pm | Sm   | Eu   | Gd   | Tb   | Dy   | Ho                         | Er                         | Tm | Yb |
| $\text{La}_2\text{Si}_3$<br>$\text{La}_2\text{Ga}_3$ | $\text{Ce}_2\text{Si}_3$<br>$\text{Ce}_2\text{Ga}_3$ | $\text{Pr}_2\text{Si}_3$<br>$\text{Pr}_2\text{Ga}_3$ | $\text{Nd}_2\text{Si}_3$<br>$\text{Nd}_2\text{Ga}_3$ |    | $\text{Sm}_2\text{Ga}_3$<br>$\text{Sm}_2\text{SnNi}_2$ | $\text{Eu}_2\text{Si}_3$<br>$\text{Eu}_2\text{Ge}_3$ | $\text{Gd}_2\text{Ga}_3$<br>$\text{Gd}_2\text{SnNi}_2$ | $\text{Tb}_2\text{Ga}_3$<br>$\text{Tb}_2\text{SnNi}_2$ | $\text{Dy}_2\text{Ga}_3$<br>$\text{Dy}_2\text{SnNi}_2$ | $\text{Ho}_2\text{SnNi}_2$ | $\text{Er}_2\text{SnNi}_2$ |    |    |

RE: Rare Earth Metals, TM: Transition Metals

Figure 15 Plot showing the wide-range occurrences of  $\text{T}_2$  phase throughout the periodic table based on the metal component (IIA-VII) and metalloid or (IB-VA) elements.

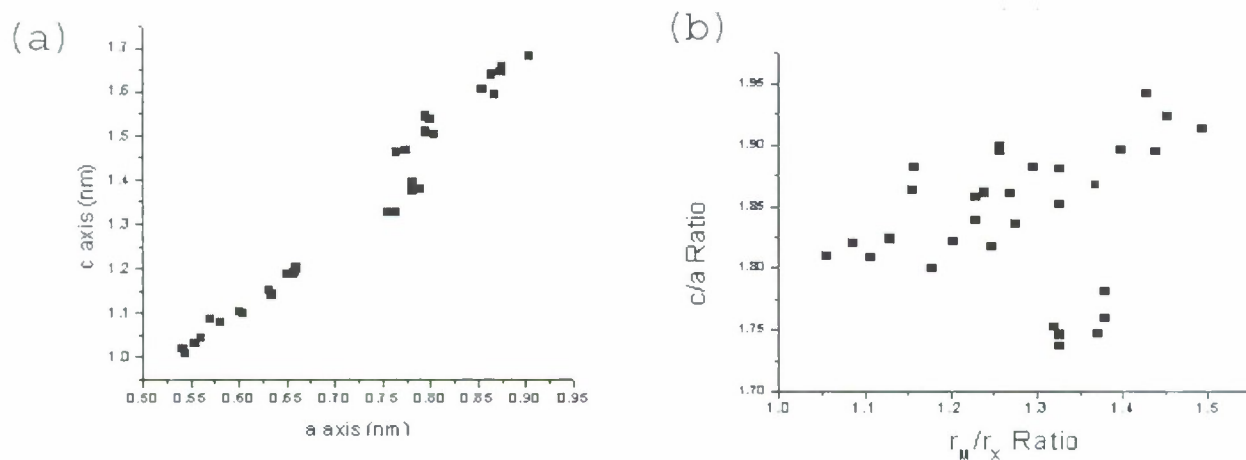


Figure 16: Plot of a) lattice dimension of c and a from known  $T_2$  compounds showing the restricted range of c/a (1.8–1.9) and b) the atomic radius ratio versus the c/a for a wide range of observed  $T_2$  phases.

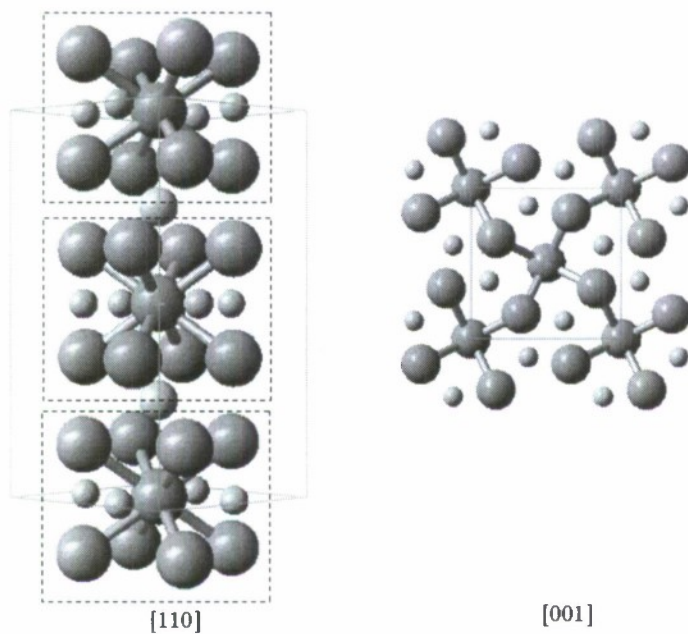


Figure 17: The Mo-Mo BCC-like clusters embedded in the  $T_2$  tetragonal crystal surrounded by the Mo-Si and Mo-B polyhedra as shown from [110] and [001] directions



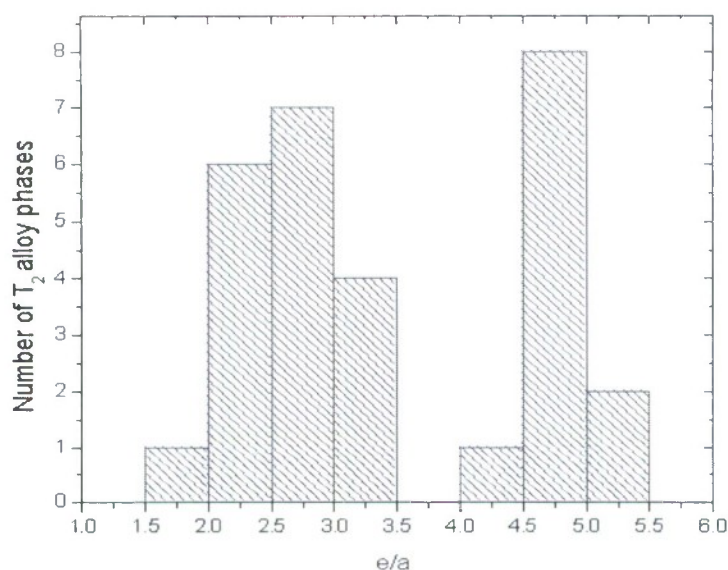


Figure 18 Plot of the occurrences of  $T_2$  phases as a function of  $e/a$  showing two distinct groups.

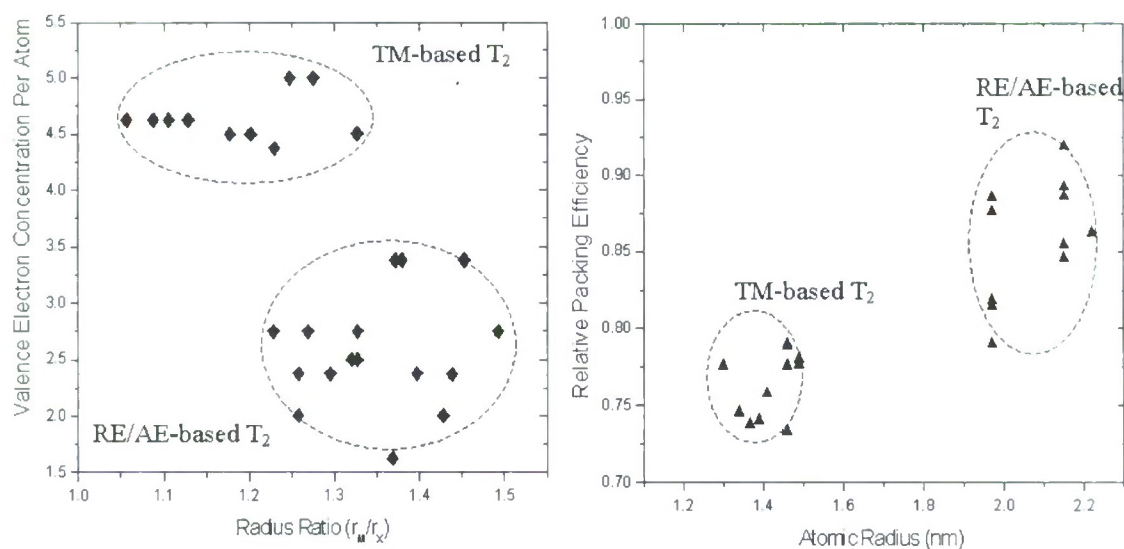


Figure 19: Plot a)  $e/a$  versus atomic radius ratio and b) packing volume fraction of the  $T_2$  crystal structures with two different base metals; Alkaline-Earth (AE) or Rare-earth (RE) metals and Transition-metals (TM). The two groups of  $T_2$  phases also have different geometric characteristics; the lower  $e/a$ , larger metal radius atom, AE/RE-based  $T_2$  phase occurs with a relatively higher radius ratio and pack density than that of the higher  $e/a$ , smaller metal radius atom, TM-based  $T_2$  phase

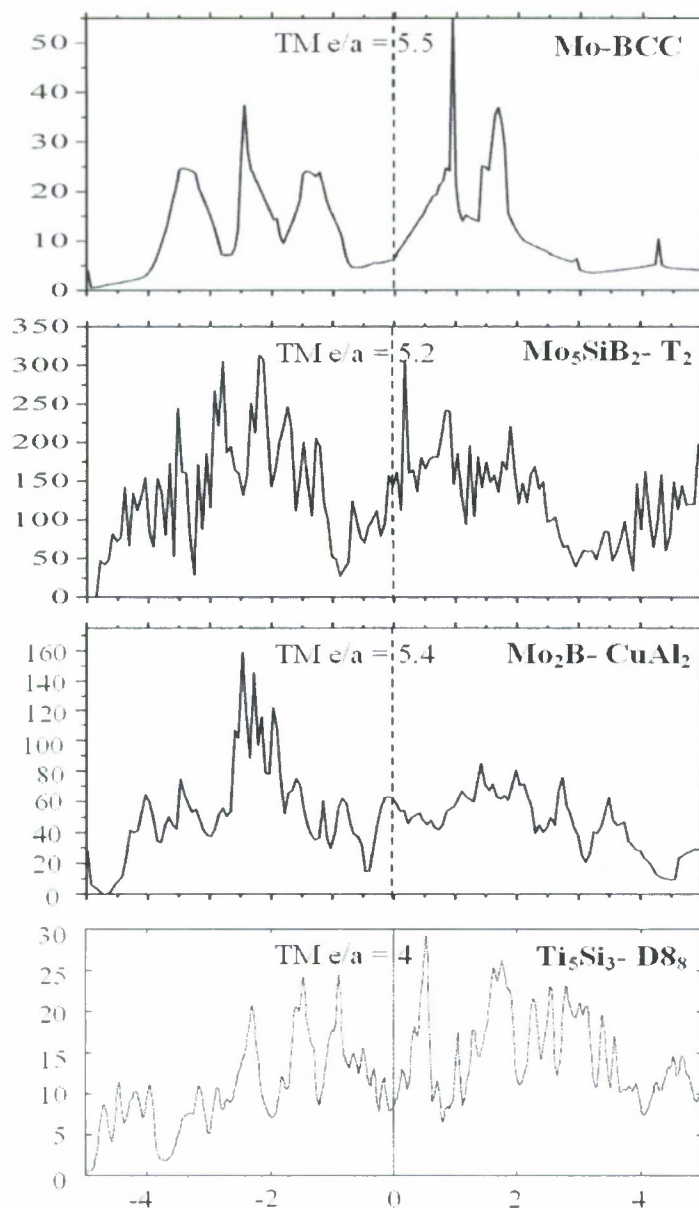


Figure 20: The Density of States of a) BCC, b) T<sub>2</sub>, c) Mo<sub>2</sub>B (CuAl<sub>2</sub>-type) and d) D8<sub>8</sub> alloy structures with their respective optimum transition metal  $e/a$  for the minimum gap position (arrow). Note the low the optimum  $e/a$  for the D8<sub>8</sub> phase (4.2) which indicates as the phase is mostly stable with the Group IVB base metals. The scale in the x axes spans from 5eV below and above the Fermi energy level that is placed at the origin.

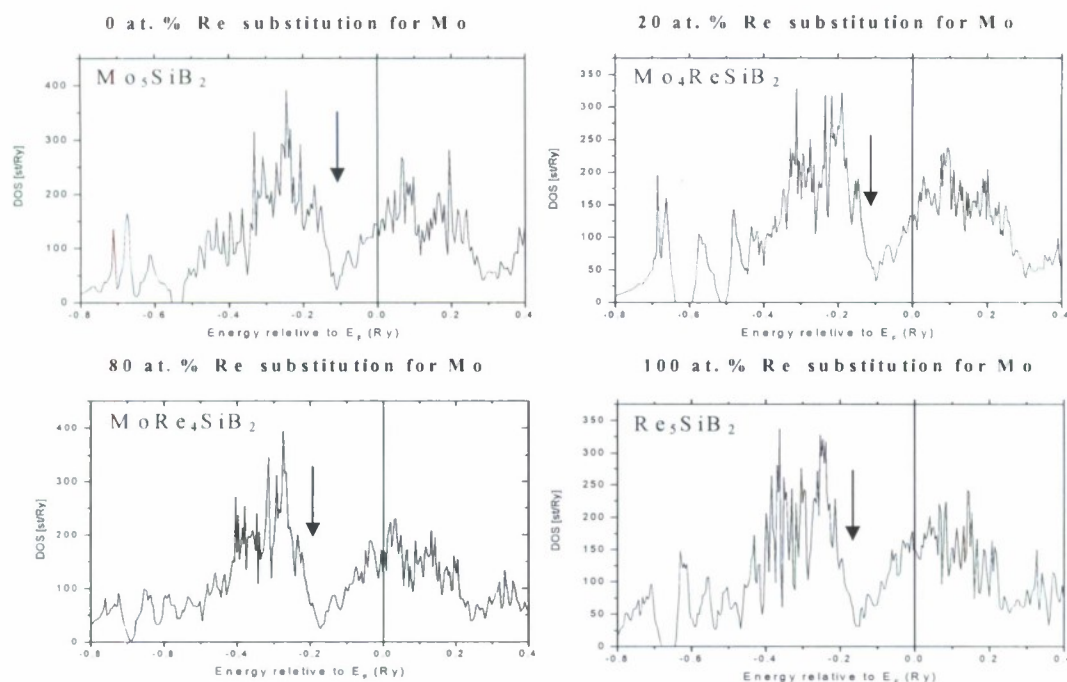


Figure 21 The Density of States of a) unalloyed  $\text{Mo}_5\text{SiB}_2$  ( $T_2$  phase), b) 20 at.% Re-alloyed c) 80 at.% Re-alloyed and d) 100 at.% Re-alloyed  $T_2$  phase showing the similarity in the characteristics of the electronic structure with a movement of the Fermi level away from the minimum gap (see arrow) due to increased valence electron concentration.

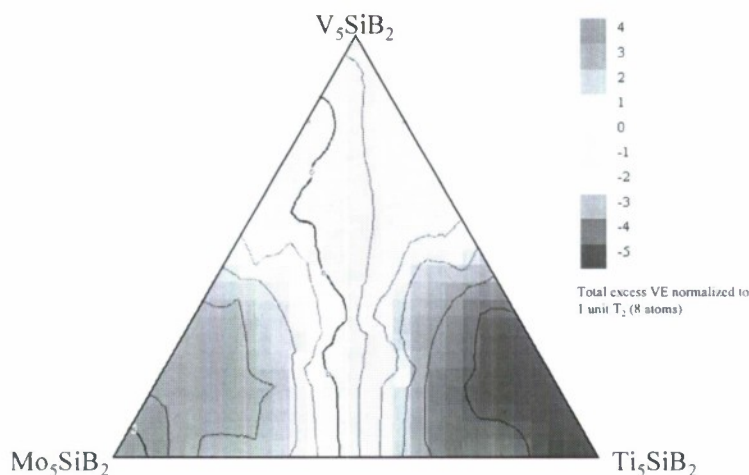


Figure 22. The excess valence electron maps of the  $T_2$  phase in five-component Mo-Ti-V-Si-B systems. Low minimum excess VE is indicative of high cohesive stability and with this approach, a concise road map for multi-component alloying strategy can be implemented. The map can be used as an effective tool to probe chemical bonding strength and relative phase stability. An expanded approach to this probing tool will be used in the proposed study to guide the defect structure engineering in BCC,  $T_2$  and  $T_1$  phases.



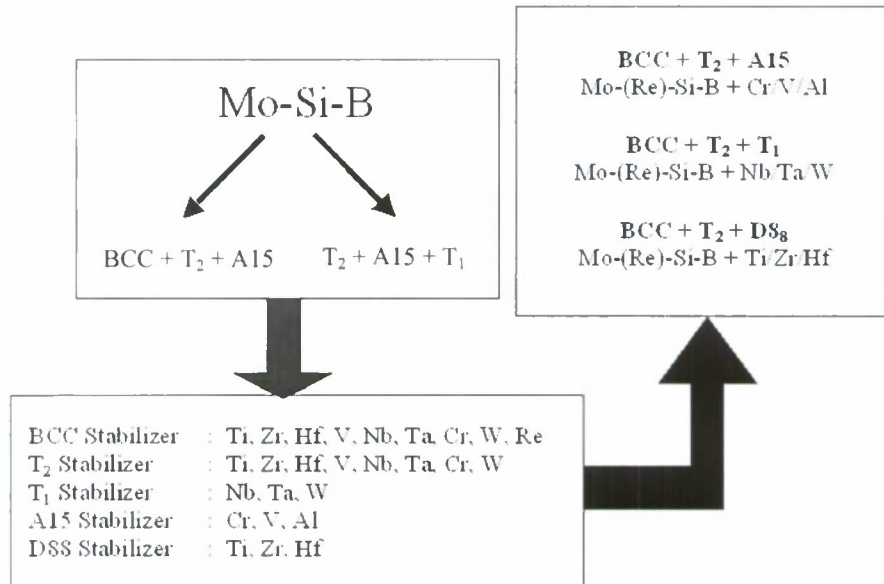


Figure 23: Alloying strategy for Mo-Si-B system based on the combined criteria for phase stability of T<sub>2</sub> phase.

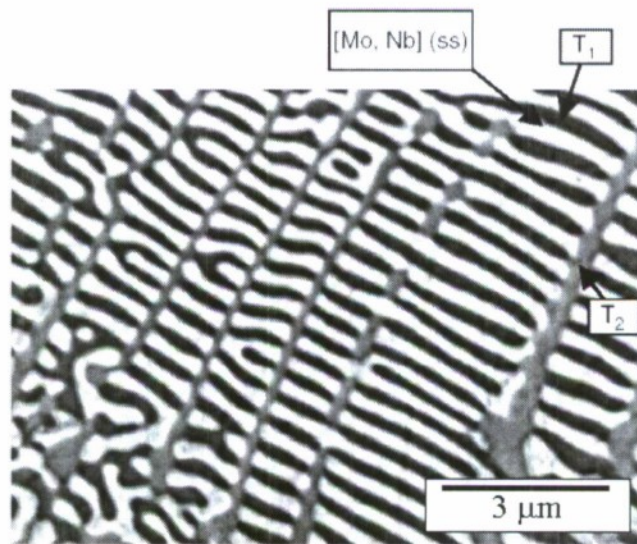


Figure 24: BSE image of the BCC + T<sub>2</sub> + T<sub>1</sub> three-phase eutectic in Mo-32.2Nb19.5Si-4.7B alloys (BCC: bright phase, T<sub>1</sub>: dark phase and T<sub>2</sub>: grey phase)

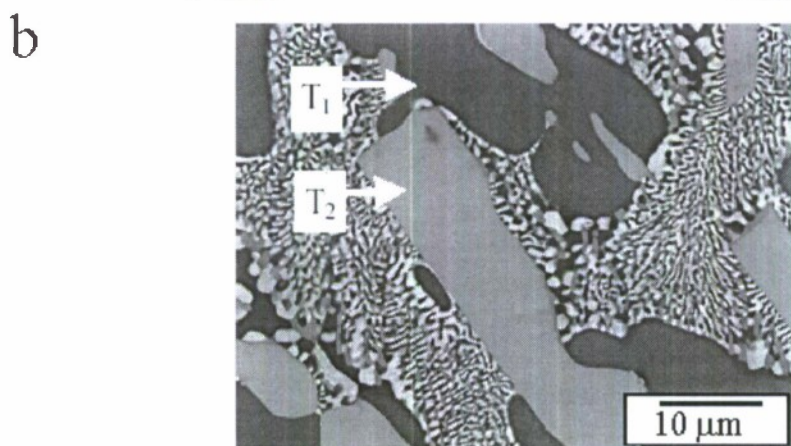
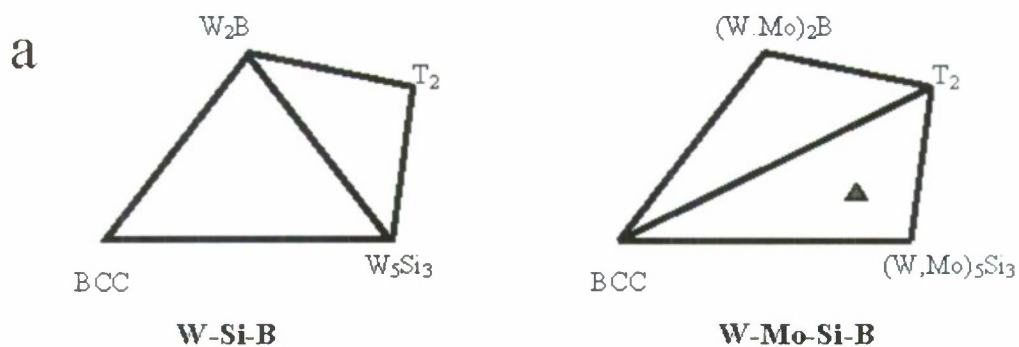


Figure 25: (a) Schematic isothermal sections to indicate that by substituting W with Mo, the stability of the two-phase field of BCC +  $T_2$  is enhanced relative to the two phase field of  $W_2B$  and  $W_5Si_3$ . Furthermore, a three-phase alloy of BCC +  $T_2$  +  $T_1$  is stabilized as exemplified in (b) with the nominal composition of Mo-7.5W-8.9B-23Si ( $\blacktriangle$ ).

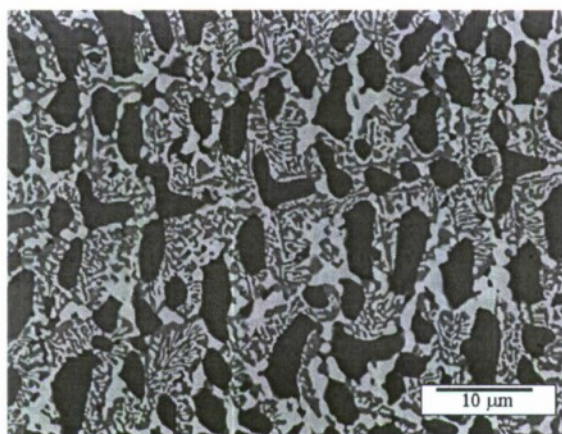


Figure 26: An example of back-scattered SEM microstructure in a three-phase BCC +  $T_2$  +  $T_1$  alloys with a nominal composition of Mo-15Re-7.5W-23Si-8.9B (at. %). Bright phase = BCC, grey phase =  $T_2$  and dark phase =  $T_1$ .



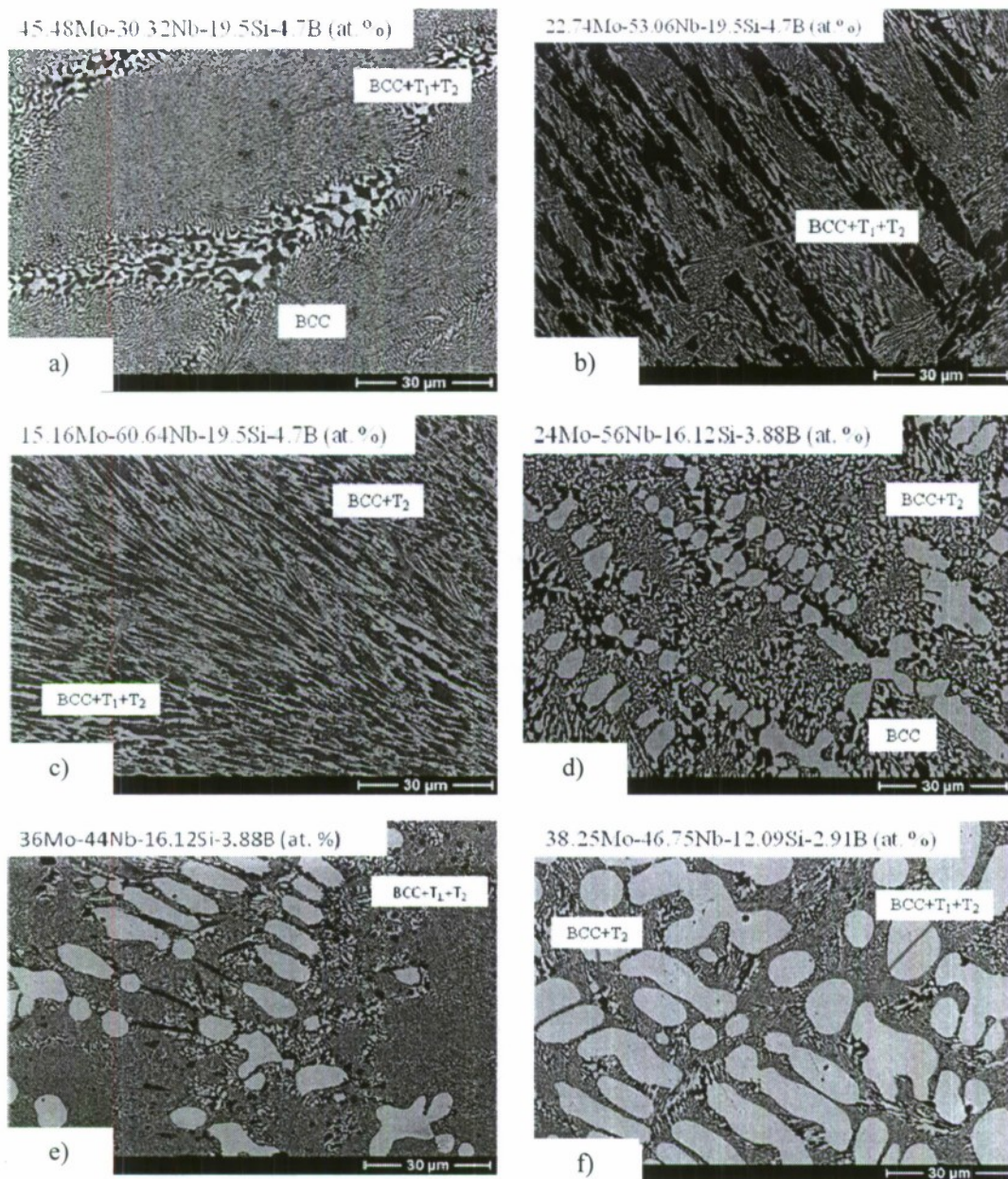


Figure 27: Mo-Nb-Si-B quaternary alloys showing a,b,c) three-phase eutectic with no BCC primary, d) Nb substitution limit resulting in a two phase alloy, and e,f) T<sub>2</sub> co-primary and three-phase eutectic.



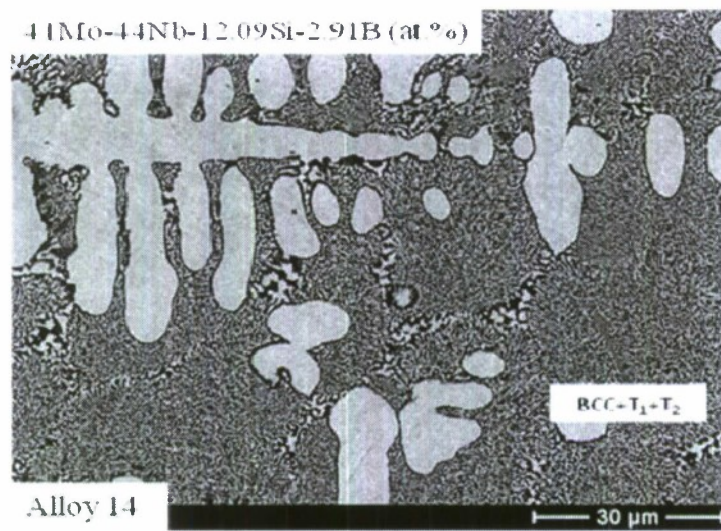


Figure 28: Mo-Nb-Si-B quaternary alloy three-phase eutectic with BCC primary.

**Program Title:** Molecular Design Of Multilayer Composites From Carbon Nanotubes

**PI:** Prof. Nicholas A. Kotov, University of Michigan, Department of Chemical Engineering, Ann Arbor, MI, 48109

**Co-PI:** Prof. John Kieffer, University of Michigan, Department of Materials Science and Engineering, Ann Arbor, MI, 48109

**Contact information:** Nicholas A. Kotov,  
Tel: 734-763-8768,  
Fax: 734-764-7453,  
E-mail: [kotov@umich.edu](mailto:kotov@umich.edu)

**Program Name:** Mechanics of Multifunctional Materials & Microsystems,  
Project Manager Dr. Les Lee

## **Final Report for 2005-2008**

### **1. Brief Description of the program and Research Approach**

Previous generation of single wall carbon nanotubes (SWNT) composites suffer from poor connectivity with, and non-uniform distribution within, a polymer matrix resulting in structural defects. These defects are responsible for the mechanical failures of SWNT-polymer composites and the lower-than-expected mechanical performance. A new processing approach, based on sequential layering of chemically-modified nanotubes and polyelectrolytes, also known as layer-by-layer assembly (LBL) can greatly diminish the phase segregation and make SWNT composite highly homogeneous. Recent results<sup>1</sup> indicate that the tensile strength of these materials is several times higher than that of SWNT composites made via mixing; it approaches values typical for hard ceramics but the material itself is significantly lighter, which makes it one of the promising candidates for aviation applications especially for unmanned aerial vehicles (UAVs).

### **2. Major Goals and Objectives.**

Our goal is to produce material with record properties using novel methods of SWNT orientation control and on-line assessment of mechanical properties of the composites. In addition to high structural uniformity provided by LBL, strengthening of bonding between graphene sheet and polymer matrix is achieved through optimization of chemical interactions of SWNT with surrounding polymer. As well, it was proposed that the orientation of the individual SWNT fibers by magnetic field will result in significant improvement of strength. Unlike any other preparation methods, LBL makes possible production of highly nano- and micro-scale optimized materials from SWNTs.

These composites are expected to have unique mechanical properties with order-of-magnitude performance improvements.

### **3. Significant Accomplishments**

1. The fundamental problem with formation of SWNT composites with high loading (70%), nanoscale uniformity, and complete exfoliation of SWNTs was resolved. No surfactants or wetting agents destroying interfacial transfer stress transfer were applied.

2. The record composites were made from SWNT stabilized by poly(styrenesulfonate) coupled with poly(vinylalcohol) by optimization of preparation conditions. The strengths obtained exceed **650 MPa**, which is an absolute record for *non-fibrous* SWNT composites. The Young's modulus exceeded **50 GPa**.

3. Mapping of the mechanical properties in respect to the
- (a) oxidation state of SWNTs
  - (b) cross-linking modality;
  - (c) SWNT loading

was carried out (Table 1). Optimum position is likely located between 55 and 70% of SWNT loading.

4. The scale-up issues were addressed in this stage of the proposal. We developed several approaches that will enable large scale and 5-30 times faster manufacturing of the LBL composites than traditional LBL: (1) dewetting method and (2) exponential growth LBL; (3) spin-assisted LBL; and (4) Large scale LBL deposition (Figure 1).

5. Method of consolidation of the LBL films in the hierarchical composites was developed (Figure 2). We observed **strengthening** of the composites as the total volume increases as opposed to decrease of the strength according to the classical  $\sigma^2 A = \text{const}$  expression. This is one of the first actual examples of **hierarchical composites**.

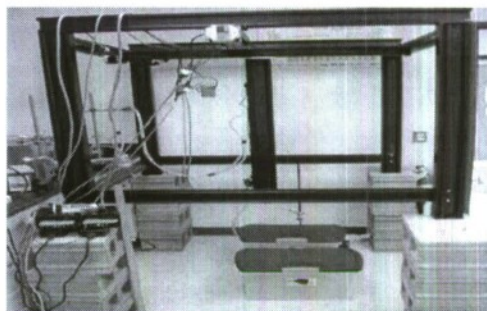


**Figure 1.** Large scale LBL deposition system, "The Big Dipper".

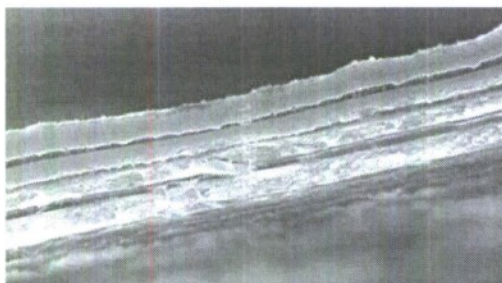


**Figure 2.** Consolidated LBL films.

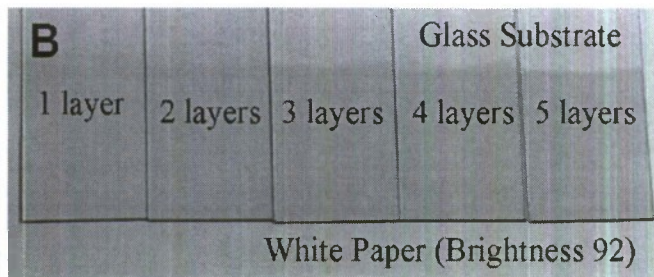


**Figure 3.** Conductive glass from SWNTs

6. We continued improving the conductivity of the LBL films of SWNT. The new method of detection of the damage in the airframe had been developed. New wireless sensors had been developed. Conductivity as high as  $5 \cdot 10^4$  S/cm was obtained. The best surface conduction was 80 Ohm per square for 80% transparency. Method of preparation of conductive glass from SWNT with tough flexible coating was found.

7. The same methods of LBL assembly developed for SWNT were applied to clays. The strongest clay composite with  $\sigma=450$  MPa and  $Y=106$  GPa was obtained. It was found that it has the ideal stress transfer even for high loadings, which is a critical fundamental discovery.



8. Method of improving fuel cell efficiency with free-standing LBL films was found.

**Table 1** Comparison table of ultimate tensile strength ( $\sigma_{ult}$ ), stiffness ( $E$ ), toughness ( $K$ ), strain ( $\epsilon$ ), and CNT loading for LBL composites and other materials.

| Samples (estimated CNT loading)                 | Cross-linkage | $\sigma_{ult}$ (MPa) | E (GPa)  | K (J/g)    | $\epsilon$ (%) |
|---|---------------|----------------------|----------|------------|----------------|
| [PVA/SWNT-COOH(15.8) +PSS] LBL (70%)            | GA            | 391.5±36.8           | 13.2±2.4 | 42.8±10.5  | 18±4           |
|   | Heat          | 359.9±41.5           | 15.1±2.8 | 41.4±7.4   | 18±3           |
|   | -             | 257.2±24.6           | 11.9±2.5 | 13.8±3.8   | 11±1           |
| PVA/SWNT-COOH(7.9) +PSS] LBL (60%)              | GA            | 504.5±67.3           | 15.6±3.8 | 121.2±19.2 | 39±3           |
|   | Heat          | 452.6±30.1           | 23.0±2.4 | 47.9±16.9  | 16±4           |
|   | -             | 224.5±15.1           | 11.6±2.0 | 26.9±10.5  | 19±7           |
| [PVA/SWNT-COOH(0) +PSS] LBL (47%)               | GA            | 233.4±25.7           | 11.3±2.0 | 11.3±5.0   | 8±3            |
|   | Heat          | 262.57±2.1           | 10.9±0.8 | 12.8±1.5   | 8±1            |
|   | -             | 196.6±30.2           | 14.2±1.7 | 5.8±3.8    | 6±2            |
| [PVA/Clay] LBL <sup>6</sup>                     | GA            | 400±40               | 106±11   | ~ 0.5      | 0.3±0.04       |
| PVA <sup>6</sup>                                | -             | 40±4                 | 1.7±0.2  | ~ 7.7      | 35±4           |
| High performance CNT fiber <sup>36</sup> (100%) | -             | 8800                 | 357      | 121        | ~8             |
| SWNT Nylon composite fiber <sup>55</sup> (0.5%) | -             | 109                  | 0.79     | 146        | 350            |
| Kevlar fiber <sup>84</sup>                      | -             | 3600                 | 90       | 33         | 5              |
| Spider silk <sup>84</sup>                       | -             | 1150±200             | 7.9±1.8  | 165±30     | 39             |
| Aluminum alloy (7075-T6)                        | -             | 572                  | 71.7     | 29         | 11             |

**People Involved:**

**Students:** Bong Sup Shim, Ken Loh, Jian Zhu, Christine Andres

**Post-docs:** Kevine Critchley.

**Future Plans:**

Preparation of large scale samples.

Manufacturing large scale samples.

Preparations parts for UAVs.

**Funding Profile:** (Give the fiscal year funding for your program to the nearest thousand dollars. For those years with no funding list it as zero. Only give the funding totals for the current AFOSR program.)

|             |             |             |             |             |             |             |
|-------------|-------------|-------------|-------------|-------------|-------------|-------------|
| <b>FY04</b> | <b>FY05</b> | <b>FY06</b> | <b>FY07</b> | <b>FY08</b> | <b>FY09</b> | <b>FY10</b> |
| 0K          | 76K         | 119K        | 123K        | 0K          | 0K          | 0K          |

**References:** (List one or two relevant publications resulting from the AFOSR funded work. If the AFOSR funded effort is new, please list one or two relevant references from your earlier work.)

Podsiadlo P., Kaushik A. K., Arruda E. M., Waas A. M., Shim B. S., Xu J., Nandivada H., Pumphlin B. G., Lahann J., Ramamoorthy A., Kotov N. A., Ultrastrong and Stiff Layered Polymer Nanocomposites, *Science*, 2007, 318, 80-83.

Michel M., Taylor A., Sekol R, Podsiadlo P., Kotov N. A. Thompson L.; High Performance, Nanostructured Membrane Electrode Assemblies for Fuel Cells Made by Layer-By-Layer Assembly of Carbon Nanocolloids, *Advanced Materials*, 2007, 19(22), 3859.

Bong Sup Shim, Zhiyong Tang, Matthew P. Morabito, Nicholas A. Kotov, Integration of conductivity, transparency and mechanical strength in highly homogeneous LBL Composites of SWNT, *Chemistry of Materials*, 2007, 19(23), 5467-5474.

Shim, B. S., Podsiadlo P., Lilly D., Agarwal A., Tang Z., Ho S., Ingle P., Patterson D., Lu W., Kotov N. A., Nanostructured Thin Films made by Dewetting Method Of Layer-By-Layer Assembly, *Nano Letters* 2007, 7(11), 3266-3273.

Loh, K. J.; Lynch, J. P.; Shim, B. S.; Kotov, N. An Optimization of Multilayer Carbon Nanotube-Polymer Composite Strain Sensors, *Journal of Intelligent Material Systems and Structures*, 2007, in press.

Podsiadlo, Paul; Sui, Lang; Elkasabi, Yaseen; Burgardt, Peter; Lee, Jaebeom; Miryala, Ashwini; Kusumaatmaja, Winardi; Carman, Mary R.; Shtein, Max; Kieffer, John; Lahann, Joerg; Kotov, Nicholas A.. Layer-by-Layer Assembled Films of Cellulose Nanowires with Antireflective Properties. *Langmuir* 2007, 23(15), 7901-7906.

Paul Podsiadlo, Zhiyong Tang, Bong Sup Shim, Nicholas A. Kotov, Counterintuitive Effect of Molecular Strength and Role of Molecular Rigidity on Mechanical Properties of Layer-By-Layer Assembled Nanocomposites, *Nano Letters*, 2007, 7(5), 1224-1231

P. Podsiadlo, Z. Liu, D. Paterson, P. B. Messersmith, N. A. Kotov, Fusion of Seashell Nacre and Marine Bioadhesive Analogs: High-Strength Nanocomposite by Layer-by-Layer Assembly of Clay and L-3,4-Dihydroxyphenylalanine Polymer, *Advanced Materials*, 2007, 19(7), 949-955.

Loh, K. J.; Kim, J.; Lynch, J. P.; Kam, N. W. S. Kotov, N. A. Multifunctional Layer-by-Layer Carbon Nanotube-Polyelectrolyte Thin Films for Strain and Corrosion Sensing, *Smart Mater. Struct.* 16 2007, 429-438